Published in : Nature Geoscience (2022), vol. 15, pp. 1048-1055
DOI: 10.1038/s41561-022-01073-3
Status : Postprint (Author's version)

Acceleration of a large deep-seated tropical landslide due to urbanization feedbacks

Antoine Dille[1,2,14], Olivier Dewitte[1], Alexander L. Handwerger[3,4], Nicolas d'Oreye[5,6], Dominique Derauw[5,7,8], Gloire Ganza Bamulezi[9,10], Guy Ilombe Mawe[9,11], Caroline Michellier[1], Jan Moeyersons[1], Elise Monsieurs[1], Toussaint Mugaruka Bibentyo[1,9,12], Sergey Samsonov[13], Benoît Smets[1,2], Matthieu Kervyn[2] & François Kervyn[1]

[1]*Department of Earth Sciences, Royal Museum for Central Africa, Tervuren, Belgium.*
[2]*Department of Geography, Vrije Universiteit Brussel, Brussels, Belgium.*
[3]*Joint Institute for Regional Earth System Science and Engineering, University of California, Los Angeles, CA, USA.*
[4]*Jet Propulsion Laboratory, California Institute of Technology, Pasadena, CA, USA.*
[5]*European Centre for Geodynamics and Seismology, Walferdange, Luxembourg.*
[6]*National Museum of Natural History, Luxembourg, Luxembourg.*
[7]*Instituto de Investigación en Paleobiología y Geología, Universidad Nacional de Rio Negro—CONICET, Río Negro, Argentina.*
[8]*Centre Spatial de Liège, Université de Liège, Angleur, Belgium.*
[9]*Département de Géologie, Université Officielle de Bukavu, Bukavu, Congo.*
[10]*Département de Géologie, Service Géologique National du Congo, Kinshasa, Congo.*
[11]*Department of Geography, University of Liège, Liège, Belgium.*
[12]*Department of Geology, Ghent University, Ghent, Belgium.*
[13]*Canada Centre for Mapping and Earth Observation, Natural Resources Canada, Ottawa, Ontario, Canada.*
[14]*Present address: Royal Belgian Institute of Natural Sciences, Operational Directorate Natural Environment, Brussels, Belgium. e-mail: antoine.dille@gmail.com; antoine.dille@africamuseum.be*

ABSTRACT

The movement of large, slow-moving, deep-seated landslides is regulated principally by changes in pore-water pressure in the slope. In urban areas, drastic reorganization of the surface and subsurface hydrology—for example, associated with roads, housings or storm drainage—may alter the subsurface hydrology and ultimately the slope stability. Yet our understanding of the influence of slope urbanization on the dynamics of landslides remains elusive. Here we combined satellite and (historical) aerial images to quantify how 70 years of hillslope urbanization changed the seasonal, annual and multi-decadal dynamics of a large, slow-moving landslide located in the tropical environment of the city of Bukavu, Democratic Republic of the Congo. Analysis of week-to-week landslide motion over the past 4.5 years reveals that it is closely tied to pore-water pressure changes, pointing to interacting influences from climate, weathering, tectonics and urban development on the landslide dynamics. Over decadal timescales, we find that the sprawl of urbanized areas led to the acceleration of a large section of the landslide, which was probably driven by self-reinforcing feedbacks involving slope movement, rerouting of surface water flows and pipe ruptures. As hillslopes in many tropical cities are being urbanized at an accelerating pace, better understanding how anthropogenic activity influences surface processes will be vital to effective risk planning and mitigation.

Published in : Nature Geoscience (2022), vol. 15, pp. 1048-1055
DOI: 10.1038/s41561-022-01073-3
Status : Postprint (Author's version)

The current rate and scale of urban growth are unprecedented in human history[1,2]. This urban transition is occurring mostly in Africa and Asia, where largely young urban landscapes expand in an informal and expansive manner[1,2]. This sprawl often overlooks natural constraints from the environment, therefore drastically increasing the population exposed to natural hazards[3,4]. On urbanized hillslopes, dozens of lives are claimed annually by shallow high-velocity landslides[4-7] whereas deeper, slow but continuously moving landslides act as a more pervasive hazard and lead to the progressive destruction of infrastructure and housing[5,8-10]. How such slow-moving, deep-seated landslides respond to natural stress perturbations (for example, seasonal[11-13] or multi-annual precipitation[14,15], seismic disturbance[16,17], undrained loading[18] or even atmospheric pressure changes[19]) has long been studied in natural environments; simplified mechanisms showing that rainfall-induced changes in pore-water pressure are principally regulating their motion[9,11-13,20-22]. Yet while hydrologists have long recognized that urbanization has dramatic impacts on catchment hydrology[23-25], very little is known about the influence of urbanization on landslide motion patterns. Quantifying how progressive hillslope urbanization changes the dynamics of deep slow-moving landslides is one of our research objectives. To this end, we study the seasonal, annual and multi-decadal dynamics of a large slow-moving landslide located in the rapidly expanding city of Bukavu in eastern Democratic Republic of the Congo (DR Congo).

Seen as a safe haven in a region where violent conflicts have forced thousands to move over the past decades, Bukavu is exemplative of those cities facing rapid and informal growth[26-28]. Originally established along the flat shoreline of the southern tip of Lake Kivu (Bukavu micro-graben[29]), the city progressively expanded on the steep slopes of the Kivu Rift[26] (Fig. 1a,b and Extended Data Fig. 1). Sited in a tropical and tectonically active landscape, where environmental conditions (climate, weathering, lithology, tectonics) are generally particularly favourable to slope failures[30,31], about one-third of the city is today built on large deep-seated landslides[32]. Most are dormant (or relict) slope failures, but portions of the city are affected by slow and continuous destruction of infrastructure and housing due to ground surface motion. One of these zones is the Funu neighbourhood. Hosting today more than 80,000 inhabitants living in overcrowded, poor-quality housing with inadequate infrastructure[26], Funu neighbourhood is built on a single slow but continuously moving landslide (Fig. 1b-e). Developed in deeply weathered tertiary and quaternary basaltic lava layers[29], this large landslide (estimated volume of ~60 ± 30 x 10^6 m^3, area of 1.6 km2 and shear surface depth estimated to vary from 30 to 80 m) is of probable seismo-tectonic origin[29] and clearly precedes human activity in the area[32]. In this Article, we present a long-term analysis of the dynamics of Funu landslide from its pre-urbanization conditions (first archives date from 1947) until today's mostly informal and extremely dense occupation. The historical, political and socioeconomic context of the country, and of this region in particular[26], have an immediate impact on availability of past knowledge and impose challenges on data collection. Therefore, we rely primarily on state-of-the-art remote sensing to apprehend constraints on deep-seated landslide processes imposed by tropical[30,31] and urban environments[33].

Published in : Nature Geoscience (2022), vol. 15, pp. 1048-1055
DOI: 10.1038/s41561-022-01073-3
Status : Postprint (Author's version)

Figure 1. *Landslides in the city of Bukavu.*

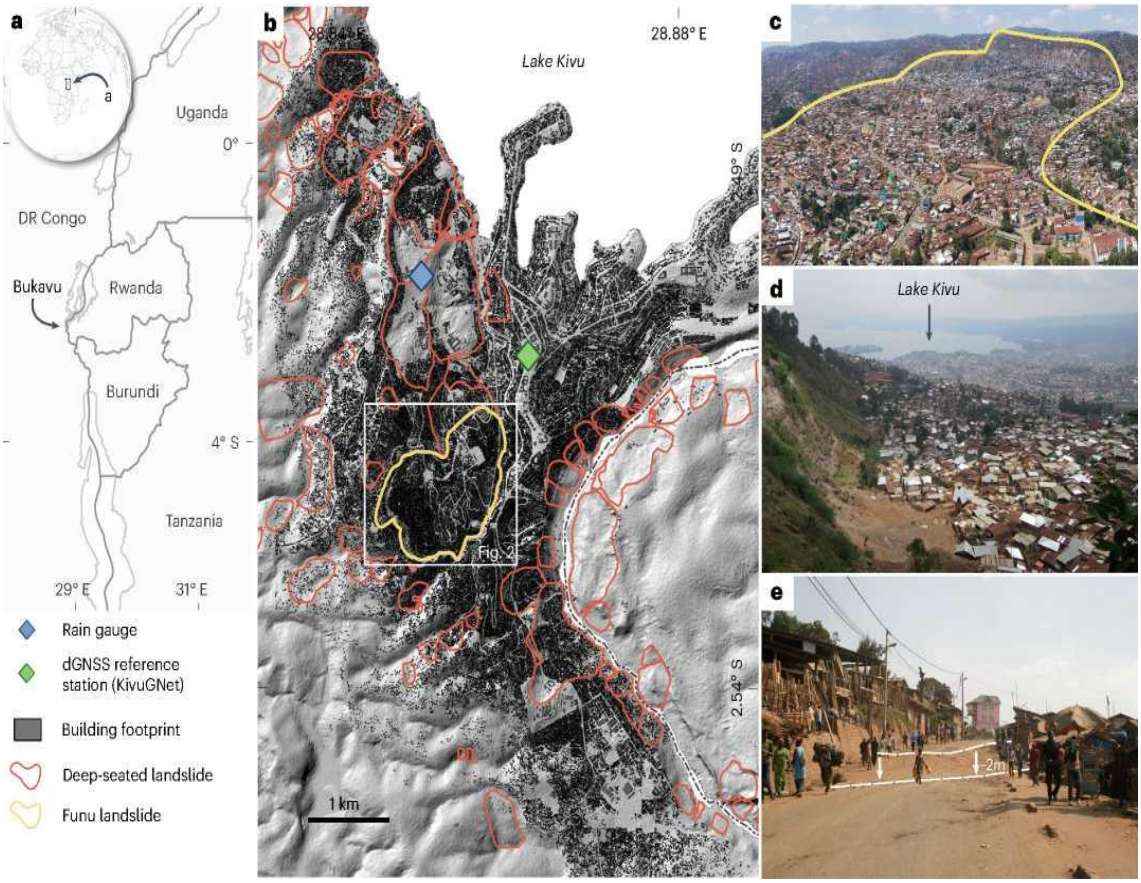

a, Location of Bukavu, DR Congo. **b**, Outlines of Funu landslide (in yellow) and other deep-seated landslides[32,58] (in red) mapped in the area. The footprints of individual buildings are shown in black. Background digital elevation model is obtained from photogrammetric processing of stereo Pléiades images from July 2013 (Methods). **c**, UAS image of Funu landslide (October 2018). **d**, View of the landslide headscarp; Lake Kivu is visible in the background. **e**, Metre-scale gap in the road illustrating the damage to infrastructure caused by continuous landslide movement. Map data in **b** © OpenStreetMap contributors.

LANDSLIDE STRUCTURE AND SEASONAL CONTROLS

We use interferometric synthetic aperture radar (InSAR) to quantify landslide motion for the period 2015-2019 (Figs. 2a-c and 3 and Extended Data Fig. 2). Using the multidimensional small baseline subset (MSBAS) method[34,35], we combine 2,575 ascending and descending interferograms from both Sentinel-1 and COSMO-SkyMed (CSK) sensors to measure two-dimensional (2D) and 3D surface motion with a sub-weekly temporal resolution (Methods). Max InSAR velocities over the landslide are 0.1 m yr^{-1} towards the east, 0.08 m yr^{-1} southwards and 0.05 m yr^{-1} vertically downwards. We also apply automated pixel tracking on Pléiades and unoccupied aircraft system (UAS) orthomosaics to measure surface displacements too large to be captured by conventional InSAR[22,35,36] (Methods). It provides velocity estimates for a relatively fast-moving 0.14 km2 zone (latter referred to as 'fastest unit') that has average and max horizontal surface velocities of 0.6 m yr^{-1} and 3 m yr^{-1}, respectively (measured for both 2013-2018 and 2017-2018 periods; Fig. 2d). Strains rates (Fig. 2e) indicate zones

Published in : Nature Geoscience (2022), vol. 15, pp. 1048-1055
DOI: 10.1038/s41561-022-01073-3
Status : Postprint (Author's version)

of stretching, shearing and shortening at the landslide surface, dominated by the deformation signal over this fastest portion of the landslide. Strong deformation gradients explain the magnitude of damages to infrastructure and housing[37] (Extended Data Fig. 3). Patterns of surface deformation and strain illustrate discontinuities and the presence of multiple morphologic and kinematic units (Extended Data Figs. 4 and 5). Common in large landslide complexes, these zones reflect spatial heterogeneity in conditions controlling landslide movement (for example, bedrock geometry, hydrological material properties and weathering[38,39]).

We use the InSAR time series to constrain the seasonal and annual dynamics of individual landslide units, sorted in three groups depending on their kinematic behaviour (Methods, Fig. 3 and Extended Data Figs. 5-7). Funu landslide moves near continuously over the year, without month(s)-long halt during the dry season[15,17], and there is no apparent minimum rainfall required to trigger landslide motion, such as observed for many landslides formed in clay-rich lithologies[40]. We find close feedbacks between changes in simulated pore-water pressure (modelled using a simple 1D hydrological model[13,15]; Methods) and landslide kinematics, which is consistent over the 4.5 years covered by our dataset (Fig. 3a-c). For all landslide units, lowest velocities are measured at the end of the dry season (September) and rise very rapidly (average time lag is 12 days; Supplementary Fig. 1) following increase in simulated pore-water pressure associated with the onset of the wet season. The landslide reaches its velocity maxima at the end of October or December depending on the location within the landslide (Fig. 3 and Extended Data Fig. 7). After a temporary decrease in velocity during the relatively drier months of January and February, a second velocity peak is observed around May (the last month of the wet season) or June-July (middle of the dry season) depending on the landslide unit, before velocities hit their minima at the end of the dry season (Supplementary Discussion). We also explore the influence of nearby medium-intensity earthquakes (moment magnitude (M_w) 4.7-5.8) on the landslide kinematics. We find no clear relation between the timing of nearby medium-intensity earthquakes (M_w 4.7-5.8) and changes in landslide motion. While the highest landslide velocities in our study period occurred following the August 2015 M_w 5.8 earthquake, the 2016 wet season was also the wettest (1,480 mm) over the observation period. More work is needed to better understand the combined role of earthquakes and precipitation, which have been shown to work together to promote instability of slow-moving landslides[17]. Following the 2016 wet season, we observe an overall decrease in landslide velocities (Extended Data Fig. 6).

The feedbacks among landslide velocity, rainfall and simulated pore-water pressure indicate that near-surface groundwater flow plays a key role in the week-to-week landslide kinematics, with increased rainfall (and related increase in pore-water pressure) resulting in low effective stress (defined as normal stress minus pore-water pressure) in the slope that promotes landslide motion[11,12]. Interestingly, rapid acceleration of the landslide occurs both at the onset of the wet season (when the groundwater table is expected to be at its lowest) and with more-intense rainy days during the wet season (when the groundwater table level is expected to be high). These changes in landslide kinematics suggest that minor changes in effective stress control changes in velocity[41], with the landslide remaining close to an acceleration thresh- old[11,12] all year long. This observation is consistent with the landslide 'bathtub hypothesis', in which landslides remain wet

Published in : Nature Geoscience (2022), vol. 15, pp. 1048-1055
DOI: 10.1038/s41561-022-01073-3
Status : Postprint (Author's version)

year-round because low-permeability shear zones prevent groundwater drainage and hydrologically isolate landslides from their surroundings[13,42].

While most studies focusing on the kinematics of deep-seated landslides showed that prolonged periods of increased precipitation were necessary to trigger acceleration at the onset of the wet season[11-13,43,44], the rapid response of Funu landslide to rainfall is surprising, notably given its large inferred depth (~30-80 m; response time is predicted to scale with depth). Such behaviour is, however, not unique[43,45], and our very high InSAR sampling frequency may also capture a response that is usually missed with lower-sampling-frequency conventional InSAR or satellite optical measurements. Yet many environmental factors—tropical climate, weathering, tectonic settings and urban development—are acting on Funu hydrology and may each influence its relatively singular kinematic response. While preferential infiltration pathways are commonly believed to play a key role in explaining rapid landslide responses[38,45,46], intense rainfall associated with tropical climate[30] may exacerbate their relative importance. Slope mechanical and hydrological properties are also known to be strongly influenced by weathering process[31,47,48], a central component of tropical geo- morphology[30]. The basaltic layers in which Funu landslide developed are a good illustration: a succession of deeply weathered quaternary and tertiary lava layers[29] with springs at various elevations (Fig. 4a) attesting to both a modified permeability and a heterogeneous alteration between landslide units. Weathering-related weakening of the slope mechanical properties and preferential infiltration pathways are probably further promoted by faulting and the long-lasting influence of recurrent seismicity[1 ,49]. All these natural constraints are commonly recognized for influencing the stability of (tropical) slopes[30,46], and we can reliably assume they act on the dynamics of Funu landslide.

The landslide cannot, however, be defined through its natural context alone. Natural lands were converted to urban lands (Fig. 1 and Extended Data Fig. 3), profoundly modifying how and where water infiltrates (for example, due to impervious surfaces, soil compaction or drainage systems) as well as the sources and locations of slope recharge (for example, additional water carried from other catchments, blockages and leaks from drainage, distribution and septic systems; Fig. 4 and Extended Data Fig. 8)[6,23,24]. These drastic and extensive reorganizations of surface and subsurface water pathways[24] lead to changes in the distribution of water within the slope, so that diffuse infiltration is largely replaced by forced point infiltration of unproportionally high water volumes on places where they do not belong naturally[6,47,50].

Altogether, urbanization results in large-scale modifications of slope groundwater[23-25], and this in turn directly affects the hillslope stress state[6,33,50,51].

We find that seasonal rainfall is the principal regulator of weekly to yearly motion of the Funu landslide. However, the infiltrating rainfall and groundwater are impacted by the local environment, including the tropical climate, rock type, tectonics and urban landscape, which all influence the slope hydrological conditions and the slope stress state. The individual roles of these parameters are difficult to disentangle over the 4.5 yr period captured by InSAR and optical imagery. Yet by looking at landslide changes over decadal timescales, which better capture the timescales of urban development, we can directly explore the influence of urbanization on the landslide behaviour.

Published in : Nature Geoscience (2022), vol. 15, pp. 1048-1055
DOI: 10.1038/s41561-022-01073-3
Status : Postprint (Author's version)

Figure 2. *Landslide motion and surface strains*

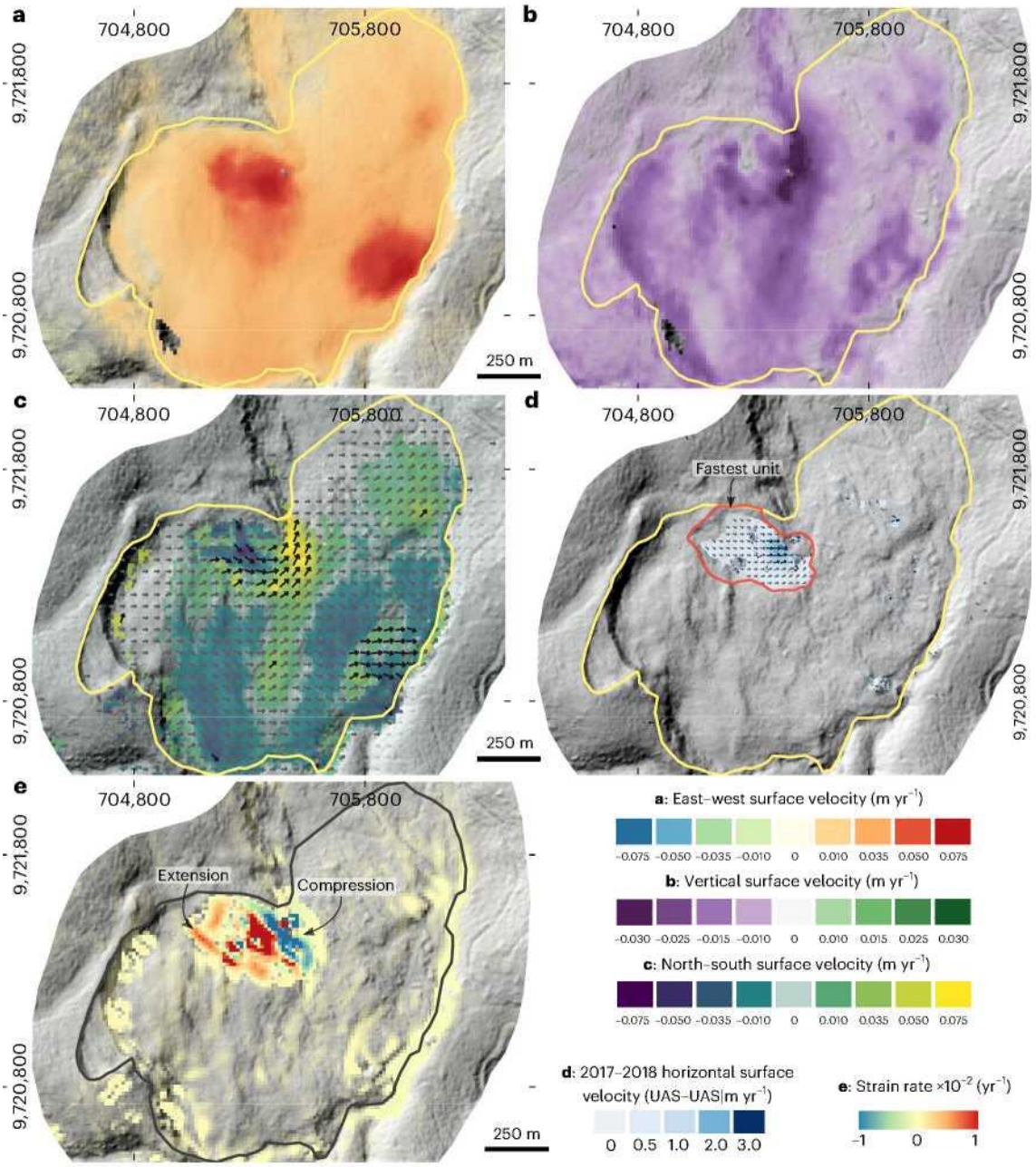

a-c, East-west (**a**), vertical(**b**) and north-south (**c**) surface velocities measured from the combined interferometric processing of CSK and Sentinel-1 images (March 2015-August 2019). Arrows in **c** illustrate the direction of surface motion from 3D InSAR. **d**, Horizontal surface velocities measured from automated pixel tracking applied to UAS structure-from-motion orthomosaics (October 2017-October 2018). **e**, Strain rates measured from combining velocity fields from SAR interferometry and automated pixel tracking. Background digital elevation model is obtained from photogrammetric processing of stereo Pléiades images from July 2013 (Methods).

Published in : Nature Geoscience (2022), vol. 15, pp. 1048-1055
DOI: 10.1038/s41561-022-01073-3
Status : Postprint (Author's version)

Figure. 3. *Landslide displacement, pore pressure and rainfall time series.*

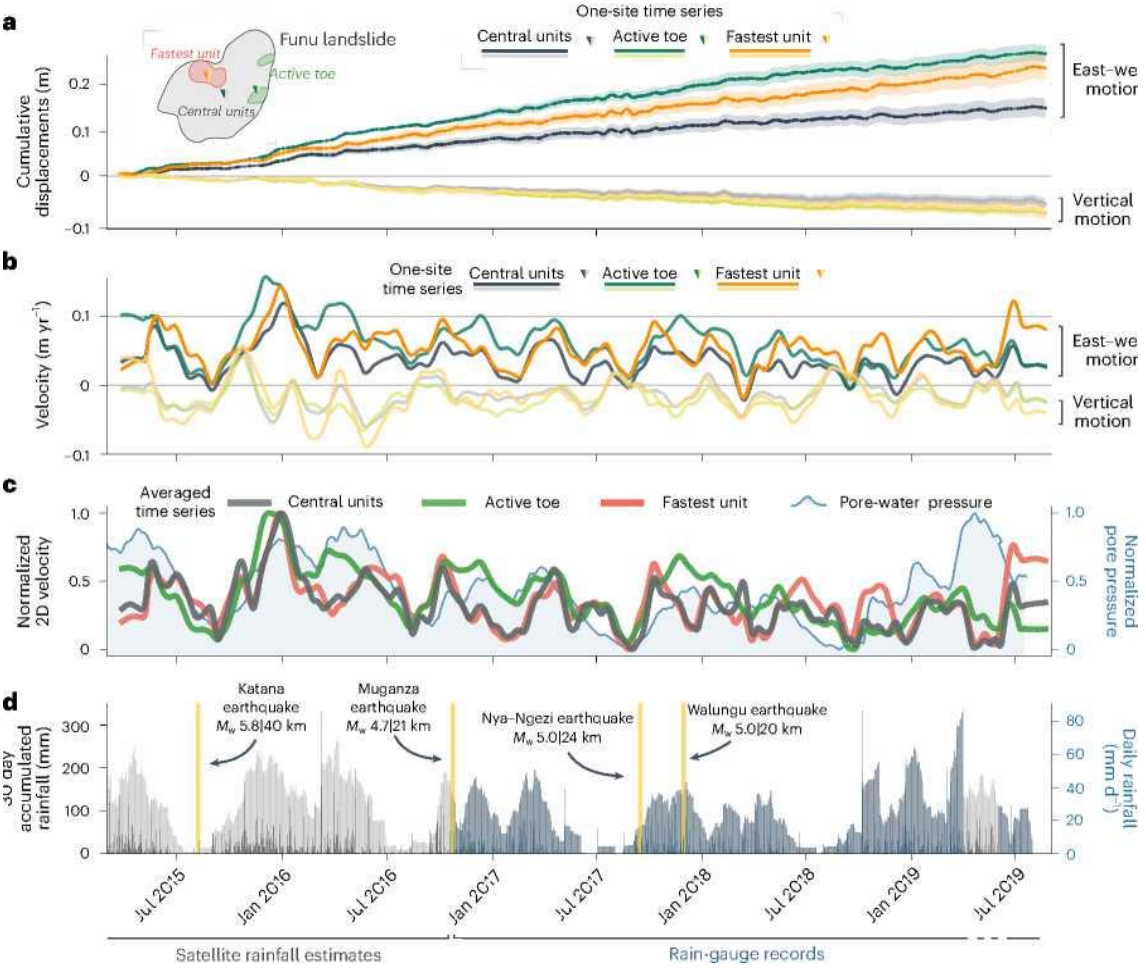

a, Eastwest and vertical cumulative displacements measured by SAR interferometry for three individual sites within the landslide (located by a triangle in subset). Uncertainties are estimated for each site from the standard deviation of the displacement measured over the four neighbouring pixels. **b**, East-west and vertical velocity time series for the same locations. **c**, Average 2D velocity time series over three different kinematic units. Time series for central units shows mean velocity from 11 individual sites, active toe from 3 sites and the fastest unit from 7 sites (Extended Data Fig. 5). Changes in velocity are compared with rainfall-induced changes in pore-water pressure simulated through a simple, homogeneous 1D diffusion model. Values are normalized to range between minimum (min = 0) and maximum (max = 1). **d**, Earthquake ($M_w \geq 4.7$) and rainfall time series for Bukavu. Rainfall data consist of rain-gauge measurements acquired ~2 km from the landslide for October 2016-April 2019, completed by satellite rainfall estimates (IMERG-GPM v.6) over the period 2000-2019. The 30-day accumulation (dark grey/blue shades) and daily rain amounts (dark grey/ blue bars) are represented.

Published in : Nature Geoscience (2022), vol. 15, pp. 1048-1055
DOI: 10.1038/s41561-022-01073-3
Status : Postprint (Author's version)

Figure 4. *Surface drainage.*

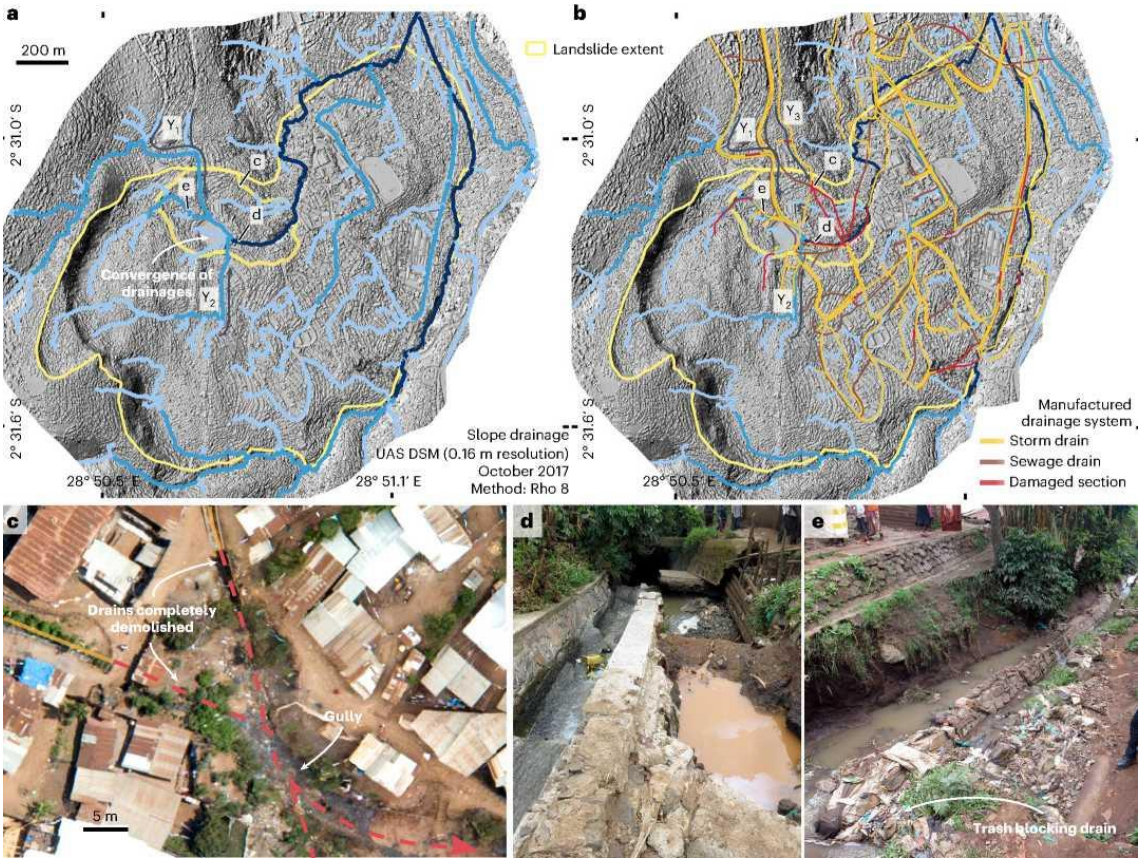

a,**b**, Slope (**a**) and artificial (storm and sewage drains) (**b**) drainage over Funu landslide. Arrows (Y*x*) highlight zones outside the natural catchment of the fastest unit from which water is conveyed by roads, housing and storm drainage systems. **c**, Example of drains destroyed by landslide motion at the edge of the fastest unit. **d,e**, Some of the many places where storm drains are inadequate, damaged and/or blocked by trash. Credit: photographs in **c**-**e**, D. Delvaux, RMCA

Published in : Nature Geoscience (2022), vol. 15, pp. 1048-1055
DOI: 10.1038/s41561-022-01073-3
Status : Postprint (Author's version)

Figure 5. *Urban growth and slope instability from 1947 to 2018.*

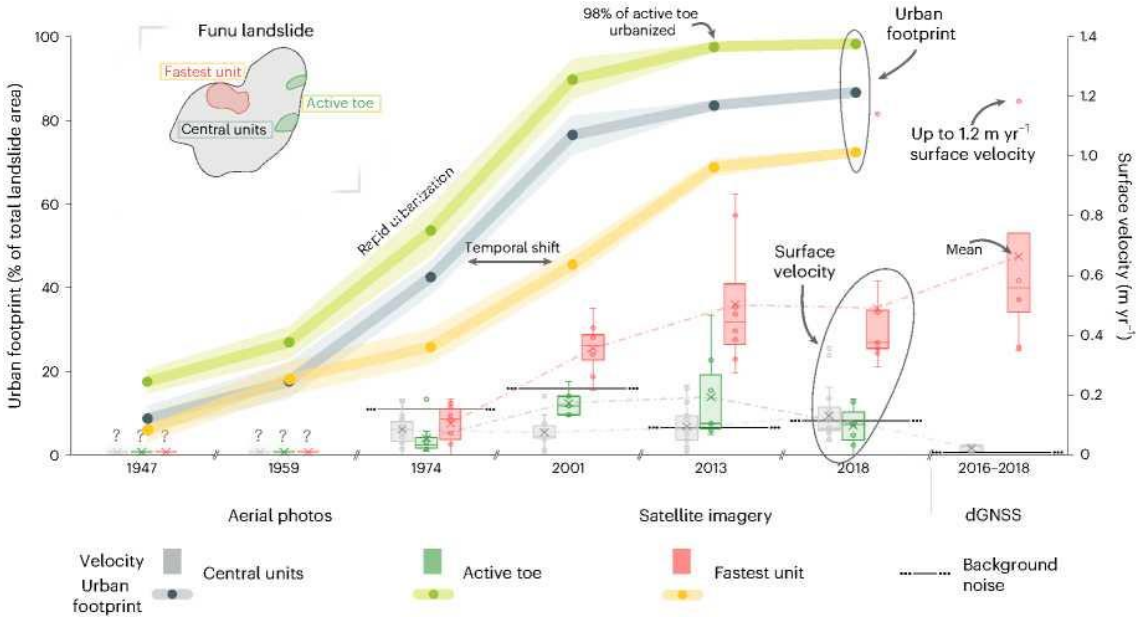

Historical aerial photos (1947, 1959 and 1974) and satellite imagery (2001, 2013 and 2018) are used to constrain velocity changes and progressive urbanization of Funu landslide (images shown in Extended Data Fig. 9). Landslide velocity and urbanization are estimated for the three kinematic units (central units, fastest unit and active toe). Surface velocity, for 1974, for example, shows average over the landslide unit for the period 1959-1974. Urbanization being limited to the toe of the landslide in 1947, surface velocities could not be estimated for the period 1947-1959. Boxes and whiskers show the distribution of velocities measured in each unit. Box bounds show lower and upper quartiles, while the mean value is expressed as an 'X' and the median as a horizontal bar. 'Background noise' represents the measured average velocity in presumably stable areas outside the landslide and is therefore considered as a proxy for noise level. Velocities from differential Global Navigation Satellite System (dGNSS) survey campaigns over 20 benchmarks are also shown for the period 2016-2018 for central and fastest units.

Published in : Nature Geoscience (2022), vol. 15, pp. 1048-1055
DOI: 10.1038/s41561-022-01073-3
Status : Postprint (Author's version)

70 YEARS OF HILLSLOPE CHANGES

To explore the impact of urbanization on tropical landslides, we analyse the multi-decadal dynamics of the Funu landslide from the earliest stages of hillslope urbanization. Urban growth (period 1947-2018) and surface motion (period 1959-2018) are quantified using historical aerial photos and very high-resolution satellite imagery (Methods, Fig. 5 and Extended Data Figs. 9 and 10). Funu landslide was progressively urbanized from its toe to its head. Located higher up in the slope, the fastest unit was thus urbanized later than the 'central units' and 'active toe', notably in the 1990s and early first decade of the 2000s, when violent conflicts and insecurity in the region drove important rural-urban migration[26-28]. All three units were moving at the same pace during the earliest stage of urbanization. While surface velocities remain relatively stable over time for both central units and active toe, we observe an acceleration of the fastest unit from the 1974-2001 period onwards. Its timing coincides with an intensification of the urbanization of the unit, but no such effect was observed for central units or active toe (Fig. 5). The urban fabric being roughly similar over the entire landslide-—dominated by light, one- to two-story wooden structures[26,37]—and the acceleration occurring while the fastest unit was only half urbanized, we hypothesize that the acceleration is the consequence of a change to the slope hydrology rather than, for example, a change due to increased loading from infrastructure (Supplementary Discussion). The rerouting of surface and subsurface water—associated with the construction of roads, housing, storm drainage and other infrastructure[23-25]—concerns all landslide units. Unlike the other two, however, the fastest unit lies at the convergence of slope drainage systems. The concentration of additional water from the establishment of new water flow paths—also conveying water from outside the natural catchment (Fig. 4a,b and Extended Data Fig. 8)—and leaks from inadequate, blocked or damaged sewage and storm drains (Fig. 4c-e) therefore added extra water to zones already closer to saturation conditions and naturally nearby to a tipping point. The destabilization of the fastest unit further caused a series of self-reinforcing feedbacks: motion favouring leaks and pipe ruptures[37], which locally promoted saturation conditions and instability. In this context, we also observe the development of deep gullies alongside the lateral margins of the fastest unit[37] (Fig. 4c and Extended Data Fig. 9). These gullies now favour both a stabilization (with the lowering of the water table) and a destabilization (due to de-buttressing) of the unit, the latter most likely playing the leading role (Supplementary Discussion). The analysis of the current landslide kinematics demonstrated how minor changes in effective stress control changes in velocity, providing essential keys to comprehend how (relatively) subtle modifications at the landslide surface may have affected the overall landslide behaviour. Further, the timing and spatial scale of the destabilization—that affects only the fastest unit and not the adjacent slopes—support the role of local-scale surface and near-surface changes associated with urbanization rather than regional-scale changes associated with seismicity and/or rainfall, the two key regional drivers that could be invoked for altering the stability conditions of the hillslope. Besides, neither changes in seismic patterns nor changes in rainfall patterns are demonstrated in the last 30+ years in the region, yet with relatively low confidence due to limited evidence[52-54].

Published in : Nature Geoscience (2022), vol. 15, pp. 1048-1055
DOI: 10.1038/s41561-022-01073-3
Status : Postprint (Author's version)

IMPLICATIONS FOR LANDSLIDE HAZARD AND MITIGATION STRATEGIES

Our findings show that urbanization can interfere with the natural behaviour of long-lived, deep-seated landslides. Such relationship is not surprising given how urbanization is known to affect slope hydrology[23-25] and how slope hydrology in turn regulates the motion of most slow-moving landslides[9,11-13,20-22]. Large slow-moving landslides are known to sometimes abruptly transition from slow motion to catastrophic failure[15,55]. Concerns are obviously higher when the landslide is embedded in a dense urban landscape. Avoidance of unstable slopes is usually not an option in developing countries, where informal urbanization generally outstrips any regulation[56]. Mitigation strategies aiming at reducing water infiltration by a comprehensive management of all forms of surface water should be backed[57]. Those are complex to implement, especially for such large landslides, and while landsliding is not the primary concern of the urban population of Bukavu (primary concerns include access to potable water, sanitation, health or education services and (food) security[26]), community-based approaches[51,57] should be promoted to prevent loss of life and infrastructure due to landsliding. As hillslopes of the world's cities are being urbanized at accelerating paces[6,7], we believe that more studies are needed to improve our understanding of how anthropogenic activity influences surface processes and landscape evolution. This would ensure the valid evaluation of landslide hazard and optimization of mitigation strategies.

ONLINE CONTENT

Any methods, additional references, Nature Portfolio reporting summaries, source data, extended data, supplementary information, acknowledgements, peer review information; details of author contributions and competing interests; and statements of data and code availability are available at https://doi.org/10.1038/s41561-022-01073-3.

METHODS

HIGH-TEMPORAL-RESOLUTION LANDSLIDE MOTION USING INSAR

We performed interferometric processing of synthetic aperture radar (InSAR) images acquired by the CSK and Sentinel-1 SAR sensors over 4.5 years (March 2015-August 2019). We generated 2,575 interferograms from 363 CSK and 227 Sentinel-1 images in both ascending and descending geometries using the MasTer Engine processing chain[59-61]. We used a multilooking factor of 5 in azimuth and range for CSK and 1 in azimuth and 7 in range for Sentinel-1 to obtain a final squared pixel size of ~15 m. Interferograms were processed with temporal baselines ranging from 2 to 80 days. A minimum coherence threshold (>0.4) was defined to avoid unnecessary processing in vegetated zones where the overall coherence is not sufficient to provide satisfactory deformation maps. The topographic phase was removed using the recent ALOS 3D DSM[62]. We processed the resulting interferograms using the MSBAS[34,35] processing chain. By combining interferograms from different SAR datasets (sensors and orbits), MSBAS provides 2D (east-west and vertical) or 3D (assuming the slide motion is parallel to the surface) displacement estimates with a combined temporal resolution[34,35]. Integrating ascending and descending CSK and Sentinel-1 images, the

Published in : Nature Geoscience (2022), vol. 15, pp. 1048-1055
DOI: 10.1038/s41561-022-01073-3
Status : Postprint (Author's version)

average number of days between two deformation measurements is down to 2.8, with a maximum of 19 days. We used measurements from differential Global Navigation Satellite System (dGNSS) survey campaigns over 20 benchmarks for validating InSAR velocities[35,36].

MEASURING RAPID LANDSLIDE MOTION

Given that displacement rates of the fastest landslide unit are above intrinsic measurement limits of conventional InSAR[22,35,36], we additionally measured landslide motion using automated pixel tracking applied on optical images. We conducted our analysis on three precisely orthorectified stereo and triplet Pléiades satellite images spanning a 5.5 yr period (March 2013, July 2013 and July 2018). Photogrammetric processing of Pléiades images (bundle adjustment, topographic surface reconstruction and orthorectification) was performed in MicMac[63], assisted with 27 ground control points (GCPs) located via dGNSS between 2014 and 2018 in the city of Bukavu and its surroundings. Alongside satellite orthomosaics, two very high-resolution digital surface models (DSMs) and orthomosaics were created from images acquired from applying structure-from-motion photogrammetry to UAS photos (UAS-SfM[64]) of Funu landslide from September-October 2017 and October 2018. Flight paths, flight speed and altitude to ground were pre-programmed to avoid/minimize motion blur and maintain a uniform ~8.2 cm pixel^{-1} ground sampling distance all along the survey area (Supplementary Table 2). Areas of 4.5 km2 (2017) and 3.5 km2 (2018) were surveyed over the 1.5 km2 size of the landslide, ensuring the presence of stable locations within the output models. In addition to Nadir views (1,750 and 490 images for 2017 and 2018, respectively), sets of 400 and 280 oblique (15-20°) images were acquired, aiming at reducing systematic DSM errors (for example, ref. [65]). UAS photogrammetric workflow was performed in Metashape Pro[66]. We used a co-alignment workflow to reduce registration errors between epochs[22,67]. The COSI CORR software package[68] was used to perform automated pixel tracking on the 0.5 m resolution Pléiades and the 0.08 m resolution UAS-SfM orthomosaics. We used decreasing window sizes (from 512 to 32 pixels) and 16-pixel steps to measure the east-west and north-south components of the surface displacement from the orthomosaics.

MORPHOLOGICAL LANDSLIDE UNITS

Most large landslides are composed of several internal units that may move semi-independently from one another. These units report evidence of internal deformation processes, and their zonation therefore helps understand the behaviour of different parts of the landslide[69,70]. We used the newly built very high-resolution UAS-SfM DSM to identify individual internal landslide units on the basis of an analysis of the landslide surface topography[69,70] (Extended Data Fig. 4.).

ESTIMATING SURFACE STRAIN AND LANDSLIDE DEPTH

Using horizontal measurements of surface motion, we estimated landslide depth and surface strain. Strain rates were measured by combining horizontal mean velocity fields from SAR interferometry (2015-2019) and automated pixel tracking for the units with fastest movements (2013-2018). Given the high spatial resolution (15 x 15 m pixels), strain rate tensor measurements are very sensitive to noise. Therefore, we used a plane-strain mass continuity equation considering a range of

Published in : Nature Geoscience (2022), vol. 15, pp. 1048-1055
DOI: 10.1038/s41561-022-01073-3
Status : Postprint (Author's version)

deformation pixels and neglecting the vertical component of motion[15]. No in situ data (for example, from geophysical measurements) are available, but proxies such as the escarpment depth (50-100 m) and the morphological study of landslide unit allowed for rough estimations of the landslide thickness[71].

TIME SERIES AND PORE-PRESSURE ANALYSIS

We extracted InSAR displacement time series over 24 sites within the landslide (Extended Data Fig. 5) to constrain velocity patterns of the individual landslide units over the four seasonal cycles (period 20152019). The 2D InSAR (east-west and up-down) was here chosen over the 3D solution for being presumably more robust for the detailed study of kinematics. In addition, neglecting the north-south component of motion has little influence considering its much lower magnitude[34]. Given the rates of deformation of the fastest landslide unit (up to 3 m yr^{-1}, a value that cannot be measured with conventional InSAR tech- nique[22] Fig. 2d), we analysed only time series of displacement extracted close to its borders, where surface velocities are of lower magnitude. To highlight the overall pattern of motion and improve the signal-to-noise ratio, we smoothed the velocity time series using a lowess filter (locally weighted linear regression) with a window size of ~90 days. While more robust than moving average, this smoothing may introduce a temporal shift to the acceleration patterns. We estimated uncertainties for each site from the standard deviation of the displacement measured over the four neighbouring pixels[72]. Times series for the 24 sites were sorted in three groups on the basis of similitude in their kinematic behaviour: the central units (13 sites), fastest unit (eight sites) and active toe (three sites) (Extended Data Figs. 5 and 7 and and Supplementary Discussion). We compared changes in landslide motion with earthquake catalogues and rainfall-induced changes in pore-water pressure that in absence of in situ measurements were simulated through a homogeneous 1D diffusion model[13,15]. We selected earthquake events powerful enough for the potential triggering of hillslope instability over Funu based on the Keefer's[73] relationship between maximum epicentral distances to landslides and earthquake magnitude. It includes seven earthquakes between M_w 4.7 and M_w 5.9 with an epicentral distance ranging from 21 to 52 km (refs. [74-76]) (Extended Data Fig. 1b). Precipitation data consist of rain-gauge measurements acquired ~2 km from the landslide for the period October 2016-April 2019 as well as version 6 of the Integrated Multi-satellite Retrievals for Global Precipitation Measurement (IMERG-GPM v.6 Final[77]) for the period 2000-2019 and validated for the region[78]. Note that IMERG-GPM data generally underestimate actual rainfall amounts[78]. Precipitation data fed a simple 1D diffusion model of pore-water pressure changes[13,15]. The pore-pressure model was run to steady state by adding 15 years of IMERG-GPM precipitation data (2000-2015) before the period of the present study (Supplementary Fig. 2). We solved for the best-fit value for landslide diffusivity by minimizing the root mean square error misfit between normalized simulated pore-water pressure and normalized average velocity time series over the landslide. For a landslide thickness of 30 m, a best-fit soil diffusivity of 1.0×10^{-4} m^2 s^{-1} generally provided good agreement between measured velocity and simulated pore-water pressure changes. This value is relatively high but falls in the range measured, for example, for landslides in weathered basalts[79]. Considering the absence ofin situ measurements and the simple approach applied, we used this pore-water pressure solution for the entire landslide. Limits of this

Published in : Nature Geoscience (2022), vol. 15, pp. 1048-1055
DOI: 10.1038/s41561-022-01073-3
Status : Postprint (Author's version)

approach are, for example, described in refs. [13,15]. In addition, since our aim is exploring timing and changes in relative strength of the pore pressure over time, only normalized velocity and pore-pressure values are compared. Values for each were normalized to range between minimum (min = 0) and maximum (max = 1).

MULTI-DECADAL ANALYSIS OF URBAN GROWTH AND SLOPE INSTABILITY

We combined historical panchromatic, ~1/50,000 scale, aerial photographs available at the Royal Museum for Central Africa (Belgium) and optical satellite images to measure landslide motion and document urban growth between 1947 and 2018 (Fig. 5 and Extended Data Fig. 9). The 1947 images originate from a scanned mosaic georeferenced using 35 GCPs located on stable ground. Orthomosaics for 1959 and 1974 were made by applying recent multiview stereo photogrammetry approaches[80] on aerial photos in Metashape Pro[66]. We used 45 and 30 GCPs for georeferencing, respectively. The GCP locations were extracted from the 1-m-resolution DSM and orthomosaic obtained from the July 2013 Pléiades stereo pair. The same DSM was used to orthorectify the 1959 and 1974 orthomosaics and a 2001 Ikonos satellite image. With additions from the 2013 and 2018 Pléiades and the 2017-2018 UAS-SfM orthomosaics, we collected images providing six windows in time to gather information on the landslide over the past 70 years.

Drastic changes in urban fabric since 1947 (Extended Data Figs. 9, 10) and differences in origin, quality and resolution of the images hampered the use of automated pixel-tracking algorithms to evaluate changes in surface velocity[81]. We therefore manually tracked the locations of identifiable benchmarks present in all images between 1959 and 2018 and distributed over the landslide to measure displacements over the years. Forty-eight benchmarks are used, representing building corners, road crossings and so on. Eleven benchmarks are located outside the landslide and 37 inside (including 8 within the fastest landslide unit and 6 within the most active sections of the landslide toe). Urbanization being limited to the toe of the landslide in 1947, surface velocities could not be estimated for the period 1947-1959. Errors in location (related to picking accuracy and orthorectification errors) are estimated to ±0.2-4.0 m. We estimated the level of background noise (for example, associated with picking errors, differences in image origin and potential inaccurate orthorectifications) from the velocity measured in the 11 presumably stable sites located outside the landslide. It varies from 0.09 to 0.18 m yr^{-1} depending on the image pairs (Fig. 5). We also manually mapped urban fabric (defined as zones with a dominance of build-up and impervious surfaces) on each image to investigate changes in the proportion of built-up area within the landslide over time. We used the same three categories (central units, fastest unit and active toe) as for the kinematic analysis. Note that the rates of displacement and the size of the fastest-moving unit prevented the use of medium-resolution satellite images (for example, Landsat and SPOT) to study their motion.

SLOPE AND MANUFACTURED DRAINAGE SYSTEMS

We modelled the slope drainage using the Rho 8 method[82] applied on the UAS DSM (October 2017; Fig. 4a). We updated the localization and condition of the storm and sewage drains (Fig. 4b) mapped

Published in : Nature Geoscience (2022), vol. 15, pp. 1048-1055
DOI: 10.1038/s41561-022-01073-3
Status : Postprint (Author's version)

for this zone of Bukavu in 2003[83] and 2017[84] combining data collected in the field and visual observations of the 0.08 m resolution UAS orthomosaics (Fig. 4c-e).

DATA AVAILABILITY

Data used in this study are available for download from https://doi. org/10.5281/zenodo.7118267. The satellite imagery that supports the findings of this study is available from the space agencies and satellite operators (ESA/Copernicus, ASI, CNES/Airbus) but restrictions apply to the availability of some of these data, which were used under license for the current study and so are not systematically available publicly. Sentinel data are made available by ESA: https://scihub.copernicus. eu/. Source data are provided with this paper.

CODE AVAILABILITY

All computer codes used in this work are available from the authors upon reasonable request.

ACKNOWLEDGEMENTS

This article is a contribution in the framework of the projects RESIST funded by the Belgian Science Policy (BELSPO), Belgium (SR/00/305) and the Fonds National de la Recherche, Luxembourg (INTER/STEREOIII/13/05/RESIST/d'Oreye); MODUS (SR/00/358), AfReSlide (BR/ 121/A2/AfReSlide) and PAStECA (BR/165/A3/PASTECA) research projects funded by BELSPO and RA_S1_RGL_GEORISK and HARISSA funded by Development Cooperation programme of the Royal Museum for Central Africa, which is supported directly by the Directorate-General Development Cooperation and Humanitarian Aid of Belgium. E.M. benefited from an F.R.S.-FNRS PhD scholarship. Part of this research was performed at the Jet Propulsion Laboratory, California Institute of Technology, under a contract with the National Aeronautics and Space Administration (80NM0018D0004). COSMO-SkyMed images were acquired through RESIST and MODUS projects as well as the CEOS Landslide Pilot. The images are under an Italian Space Agency (ASI) licence. Special thanks go to Université Officielle de Bukavu, and particularly to the members of the Department of Geology. Together with the support of the Civil Protection of South Kivu, they made it possible to execute fieldwork in the study area and provided crucial help for the dGNSS acquisition campaigns and the many discussions on landslide processes in the area. We thank D. Delvaux for sharing field pictures and discussions on the tectonics and geology of the area. We further thank G. Bennett, P. Gonzalez, J.-P. Malet and M. Rutzinger for their insightful discussions and recommendation regarding this research.

AUTHOR CONTRIBUTIONS

A.D. and O.D. conceived the study with inputs from F.K. and M.K.. A.D. processed and analysed the data and created the figures. A.D. wrote the manuscript, with main inputs from O.D. and key contribution from M.K. and A.L.H. A.D., O.D., F.K., G.B.G., G.I.M., E.M. and T.M.B. participated in the field-data acquisition and interpretation. C.M. and J.M. participated in the interpretation of the field data. N.d'O., D.D., S.S. and B.S. assisted with the processing of SAR and UAS data. A.L.H. assisted

Published in : Nature Geoscience (2022), vol. 15, pp. 1048-1055
DOI: 10.1038/s41561-022-01073-3
Status : Postprint (Author's version)

with the processing of slope pore-water simulations. All the authors contributed to the final version of the paper. O.D. and F.K. coordinated and designed this collaborative study in the frame of the RESIST and MODUS projects.

COMPETING INTERESTS

The authors declare no competing interests.

ADDITIONAL INFORMATION

EXTENDED DATA is available for this paper at https://doi.org/10.1038/s41561-022-01073-3.

SUPPLEMENTARY INFORMATION The online version contains supplementary material available at https://doi.org/10.1038/s41561-022-01073-3.

PEER REVIEW INFORMATION *Nature Geoscience* thanks Joanne Wood and the other, anonymous, reviewer(s) for their contribution to the peer review of this work. Primary Handling Editor: James Super, in collaboration with the *Nature Geoscience* team.

REPRINTS AND PERMISSIONS INFORMATION is available at www.nature.com/reprints

Published in : Nature Geoscience (2022), vol. 15, pp. 1048-1055
DOI: 10.1038/s41561-022-01073-3
Status : Postprint (Author's version)

Extended Data Figure 1. *Regional context and overview of the city of Bukavu.*

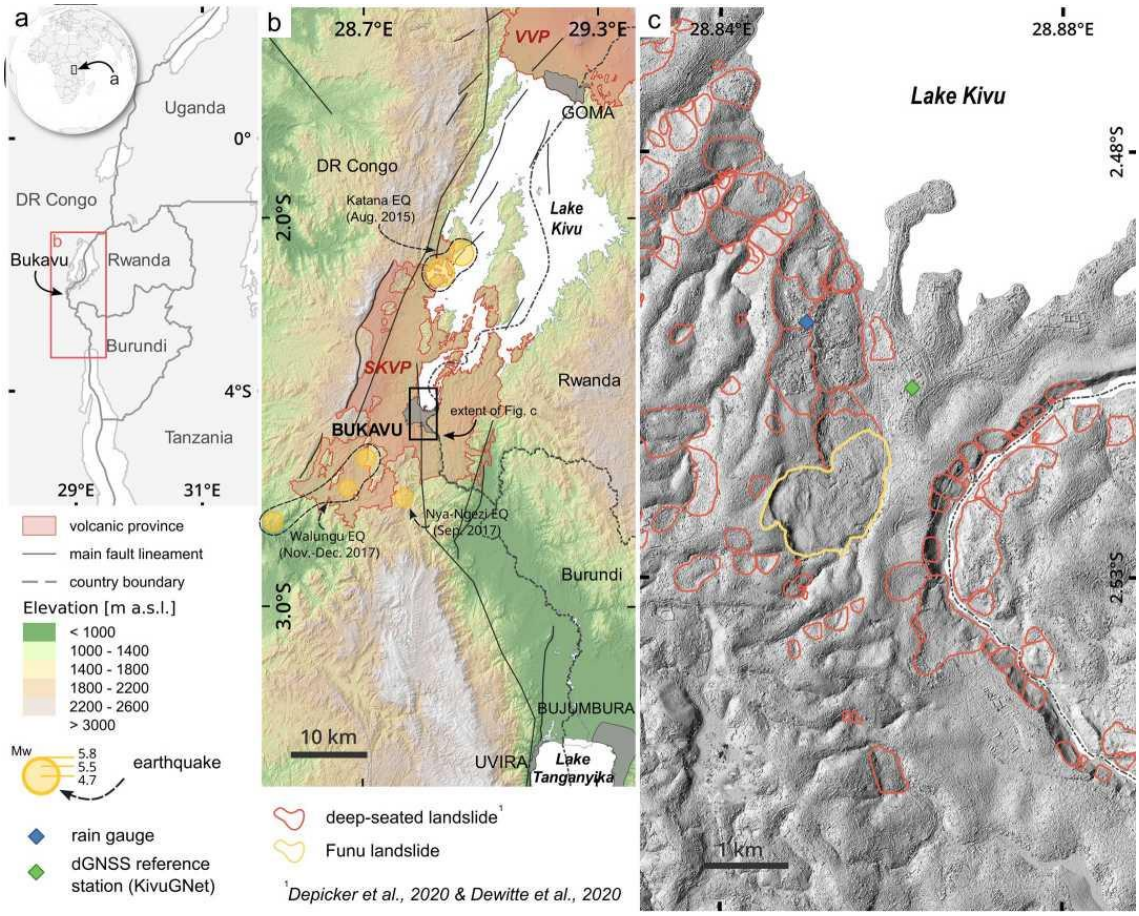

a, Location of Bukavu, DR Congo. **b**, The Kivu Rift, showing main fault lineaments, the South Kivu Volcanic Province (SKVP) and the location of the main earthquakes that occurred during the period 2015-2019. **c**, Outlines of Funu landslide (in yellow) and other deep-seated landslides10,11 (in red) mapped in the area. Background digital elevation model is obtained from photogrammetric processing of stereo Pléiades images from July 2013 (see Methods)

Published in : Nature Geoscience (2022), vol. 15, pp. 1048-1055
DOI: 10.1038/s41561-022-01073-3
Status : Postprint (Author's version)

Extended Data Figure 2. *Surface deformation maps over the city of Bukavu.*

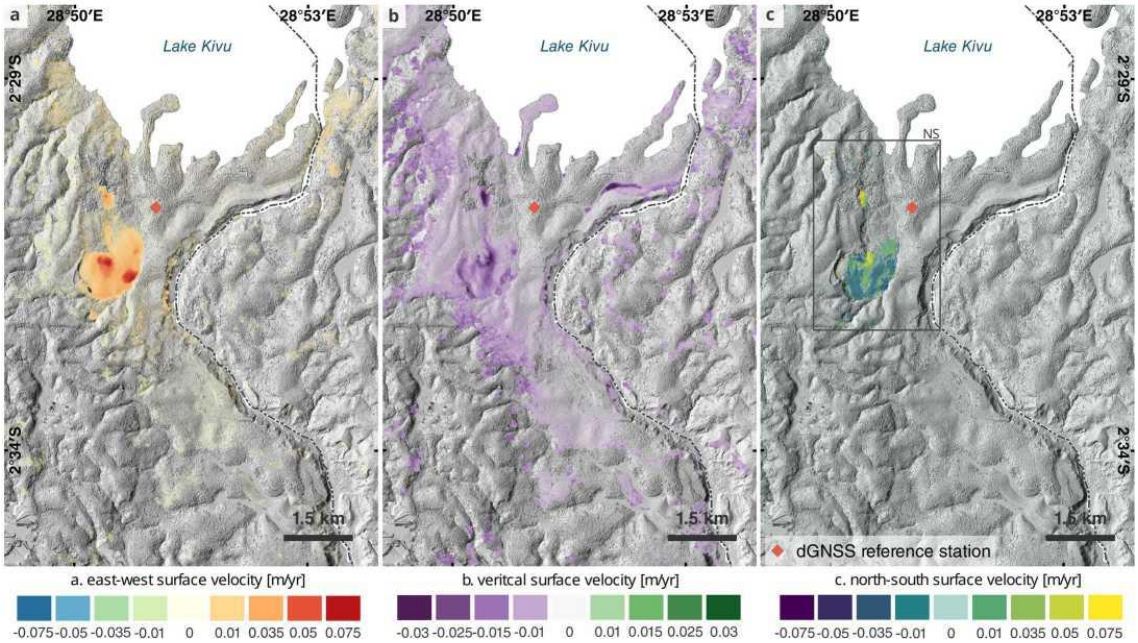

a, East-west, **b**, vertical and c, north-south surface velocities measured from combined interferometric processing of CSK and Sentinel 1 images. Background digital elevation model is obtained from photogrammetric processing of stereo Pléiades images from July 2013 (see Methods).

Published in : Nature Geoscience (2022), vol. 15, pp. 1048-1055
DOI: 10.1038/s41561-022-01073-3
Status : Postprint (Author's version)

Extended Data Figure 3. *Urban density and landslide impacts.*

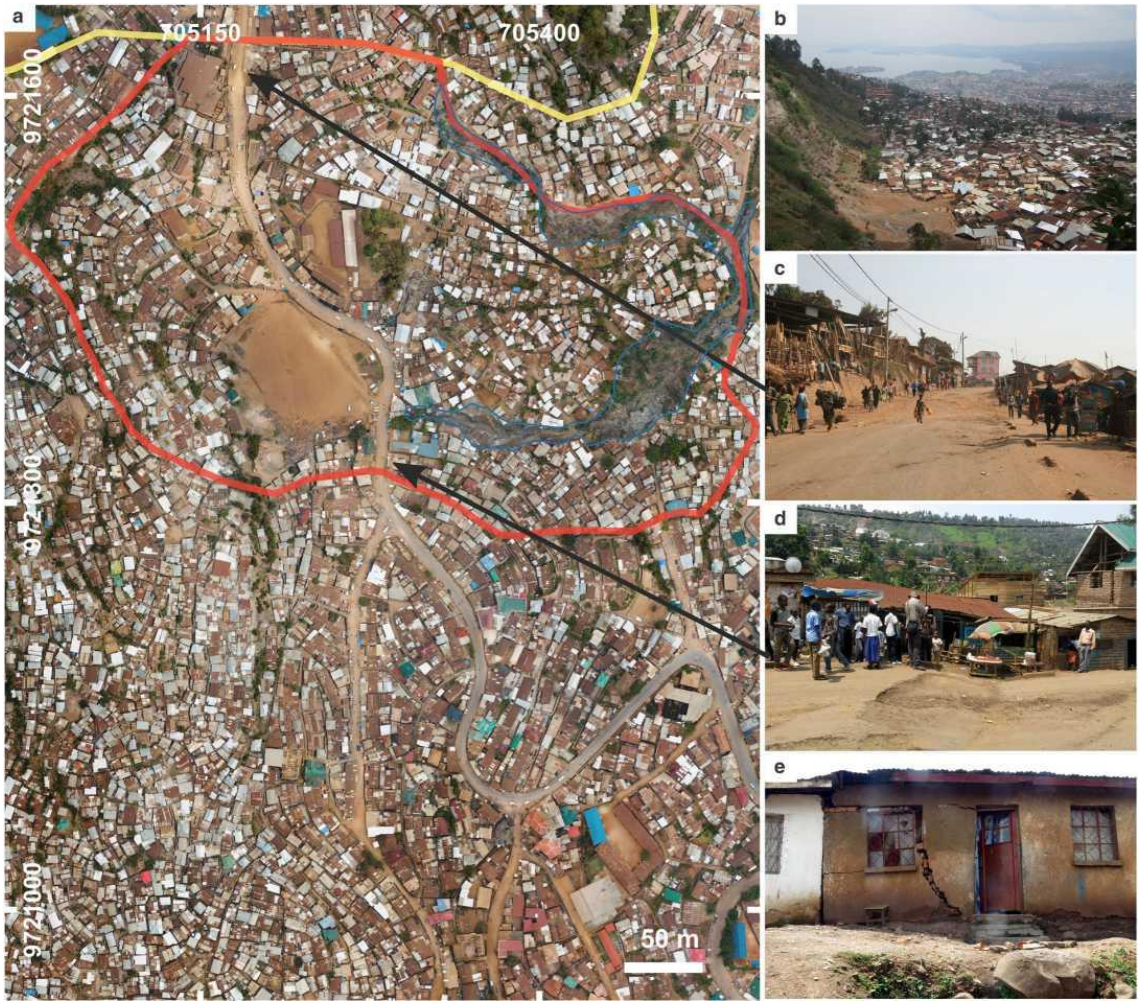

a, Very-high resolution UAS-SfM orthomosaic (Oct. 2018) of a section the landslide that includes the 14-ha 'fastest unit' (in red). Note the very-high density of individual building (the landslide population is estimated to ~55 000 inhab./km2[4]). In blue is highlighted the extent of the two gullies that partially delimit the toe of the fastest unit. **b**, View of the landslide taken from the headscarp. Lake Kivu is visible in the background. **c**, and **d**, damages to a road at the border of the fastest unit, where velocity gradients are the highest. **e**, damages to a house within the landslide. Extent of **a**, is shown in Extended Data Fig. 4.

Published in : Nature Geoscience (2022), vol. 15, pp. 1048-1055
DOI: 10.1038/s41561-022-01073-3
Status : Postprint (Author's version)

Extended Data Figure 4. *Morphological landslide units.*

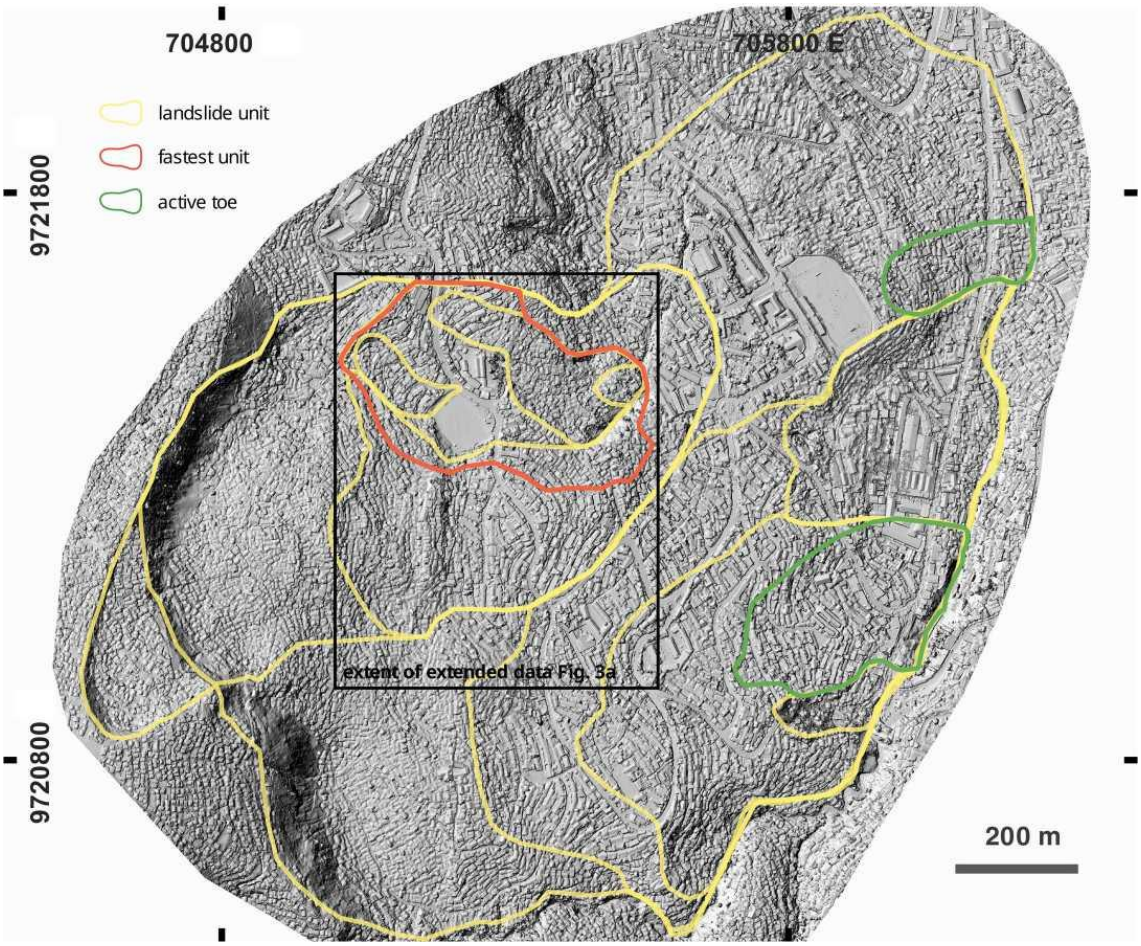

Very-high resolution shaded relief of the landslide obtained from UAS-SfM (Oct. 2017) on which are outlined the different landslide morphologic units. In green and red are shown the 'fastest unit' and the 'active toe' units, grouped based on their kinematic behaviour. Note the dense urban fabric.

Published in : Nature Geoscience (2022), vol. 15, pp. 1048-1055
DOI: 10.1038/s41561-022-01073-3
Status : Postprint (Author's version)

Extended Data Figure 5. *Sites of displacement time series.*

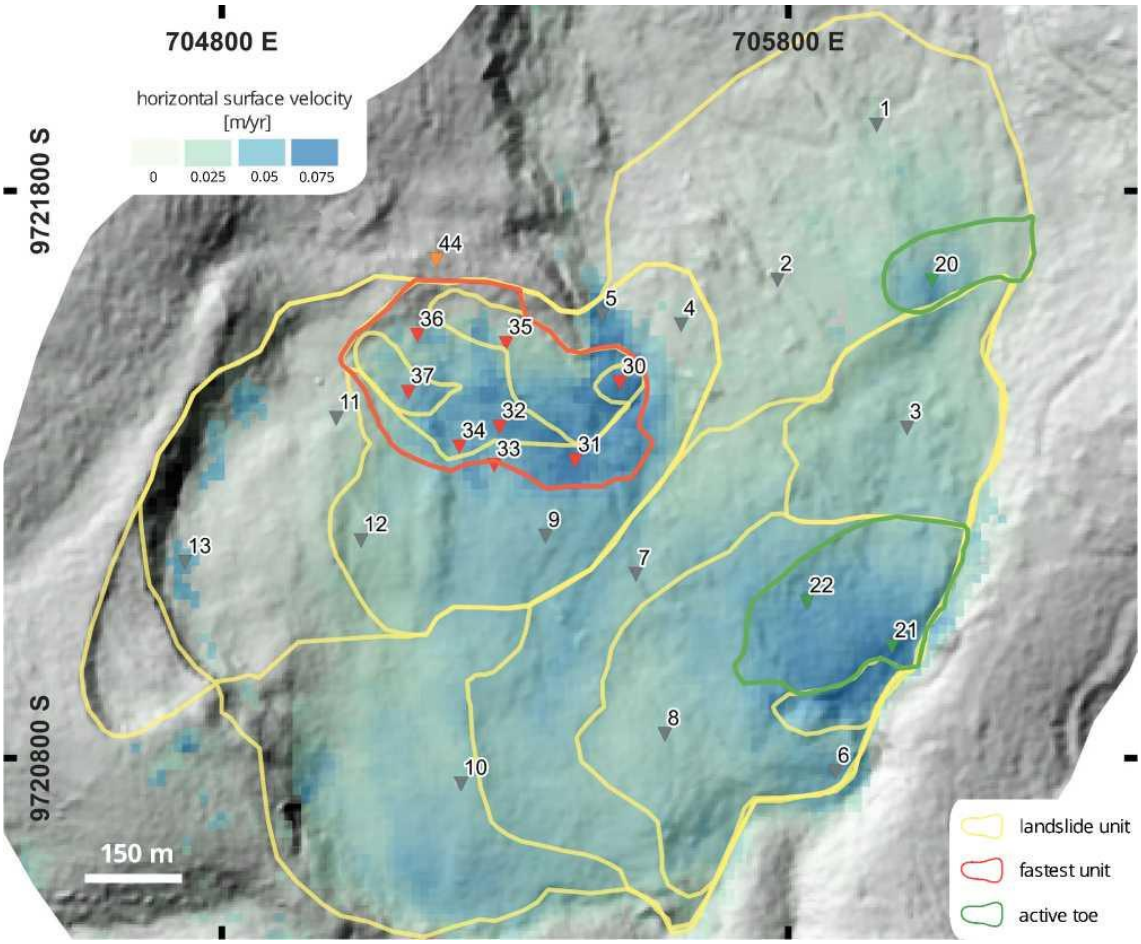

Location of the sites where InSAR displacement time series were extracted. In red are shown sites located in and grouped as 'fastest unit' (8 sites), in green the 'active toe' (3 sites) and in grey the 'central units' (13 sites).

Published in : Nature Geoscience (2022), vol. 15, pp. 1048-1055
DOI: 10.1038/s41561-022-01073-3
Status : Postprint (Author's version)

Extended Data Figure 6. *Seasonal deformation pattern.*

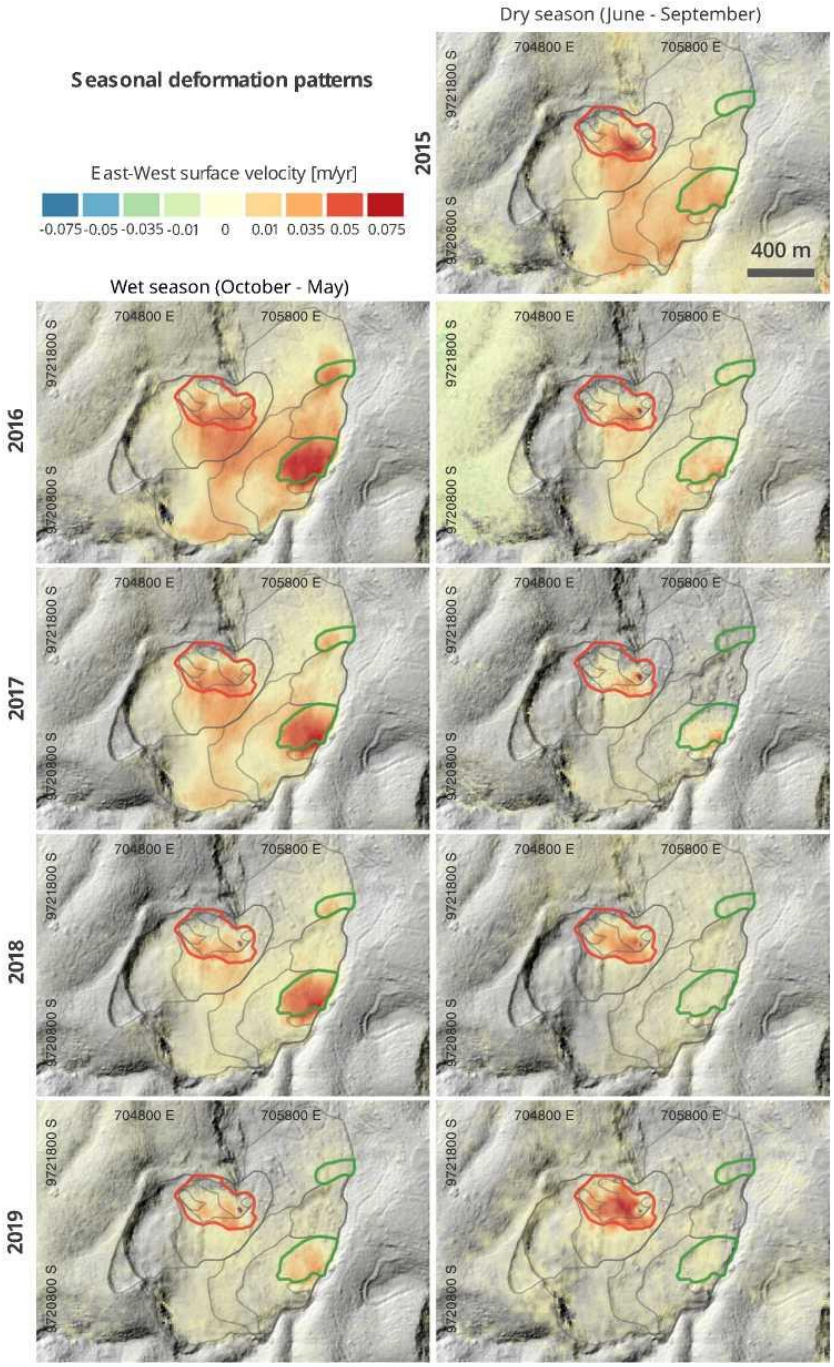

East-west surface velocities are measured by InSAR for each season (defined as dry from June to September and wet from October to May). The 'fastest unit' is outlined in red and the 'active toe' in green.

Published in : Nature Geoscience (2022), vol. 15, pp. 1048-1055
DOI: 10.1038/s41561-022-01073-3
Status : Postprint (Author's version)

Extended Data Figure 7. *Monthly landslide velocities.*

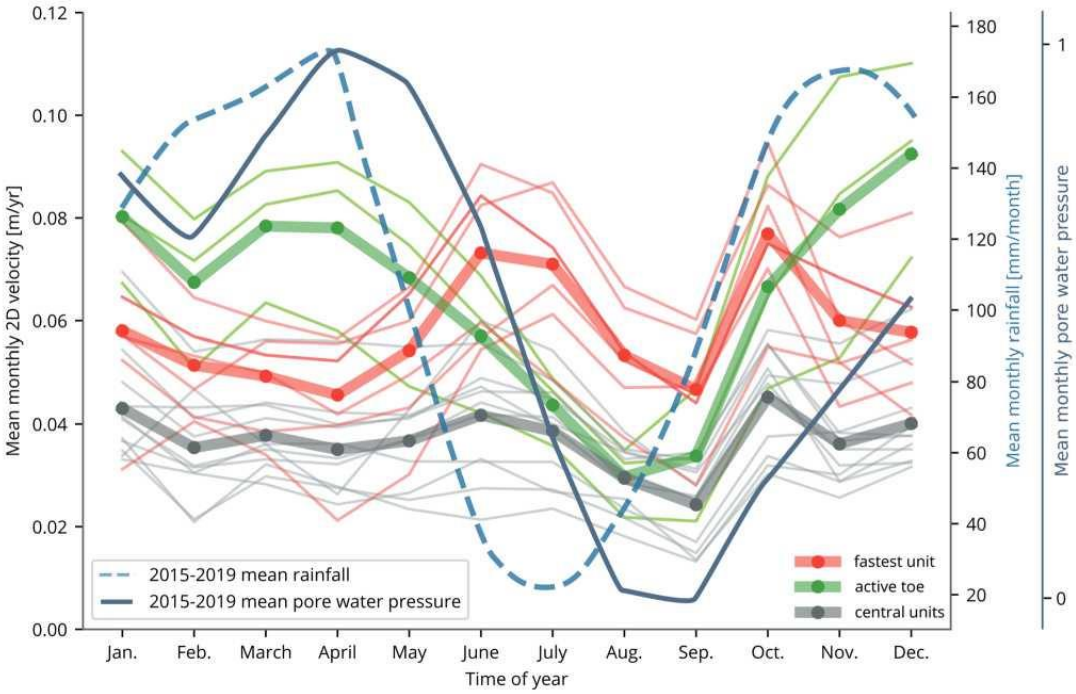

2D InSAR velocities (east-west and vertical) averaged by months for the period 2015-2019. Thick lines represent mean 2D velocity time series from all sites in landslide 'active toe', 'fastest unit' and the landslide 'central units' (see Extended Data Fig. 5 for sites locations). The 2015-2019 mean monthly rainfall and simulated pore water pressure in the slope are displayed. A detailed analysis of the different seasonal velocity patterns for the different landslide units is provided as supplementary discussion (1.1).

Published in : Nature Geoscience (2022), vol. 15, pp. 1048-1055
DOI: 10.1038/s41561-022-01073-3
Status : Postprint (Author's version)

Extended Data Figure 8. *Simulations of slope surface drainage.*

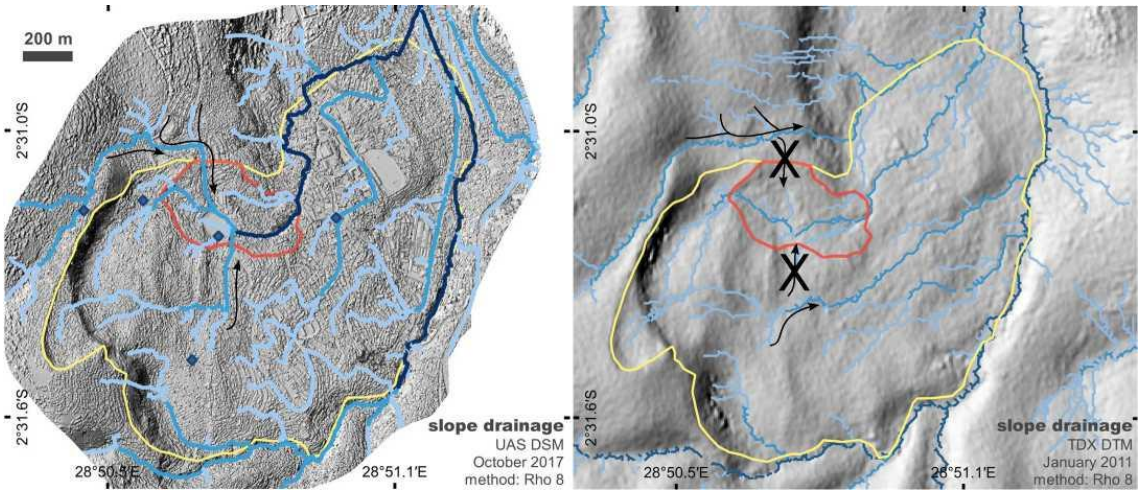

a, Slope surface drainage over Funu landslide simulated on very-high-resolution UAS-SfM DSM. Arrows highlight zones outside the natural catchment of the 'fastest unit' (in red) from which water is conveyed by man-made infrastructure. Blue diamonds show the location of springs. **b**, Slope surface drainage simulated on a Digital Terrain Model (where the influence of artificial infrastructures is assumed negligeable).

Published in : Nature Geoscience (2022), vol. 15, pp. 1048-1055
DOI: 10.1038/s41561-022-01073-3
Status : Postprint (Author's version)

Extended Data Figure 9. *Progressive urbanisation of Funu landslide.*

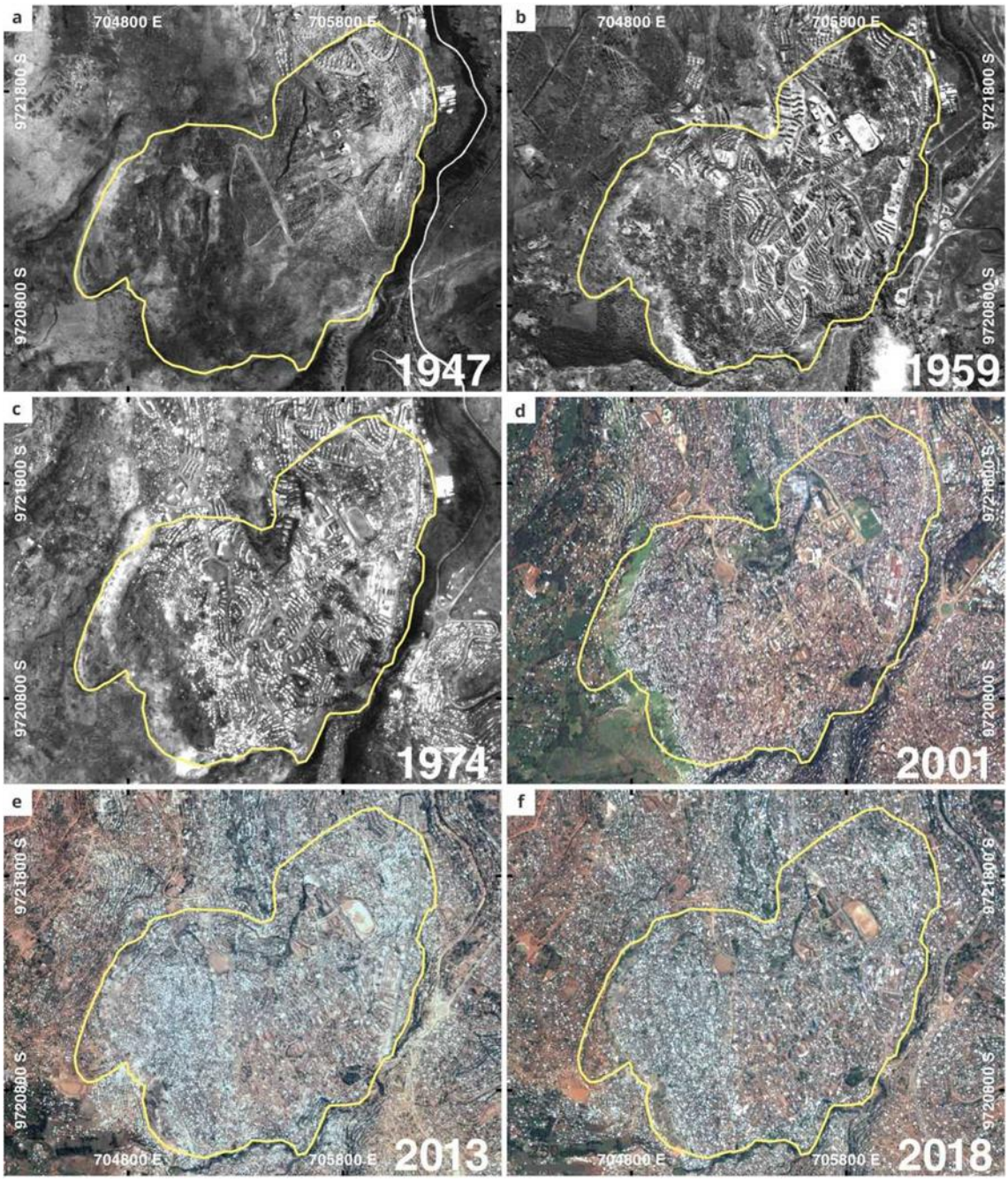

Aerial and satellite images of Funu landslide for the period 1947 until 2018. 1947, 1959 and 1974 are derived from historical aerial images available at the Royal Museum for Central Africa (Belgium). 2001 is an Ikonos satellite orthomosaic and 2013 and 2018 are very-high resolution Pléiades orthomosaics. These images were used in the evaluation of the changes in landslide motion and urban fabric over the last 70 years (Fig. 5).

Published in : Nature Geoscience (2022), vol. 15, pp. 1048-1055
DOI: 10.1038/s41561-022-01073-3
Status : Postprint (Author's version)

Extended Data Figure 10. *Urban development at Funu landslide.*

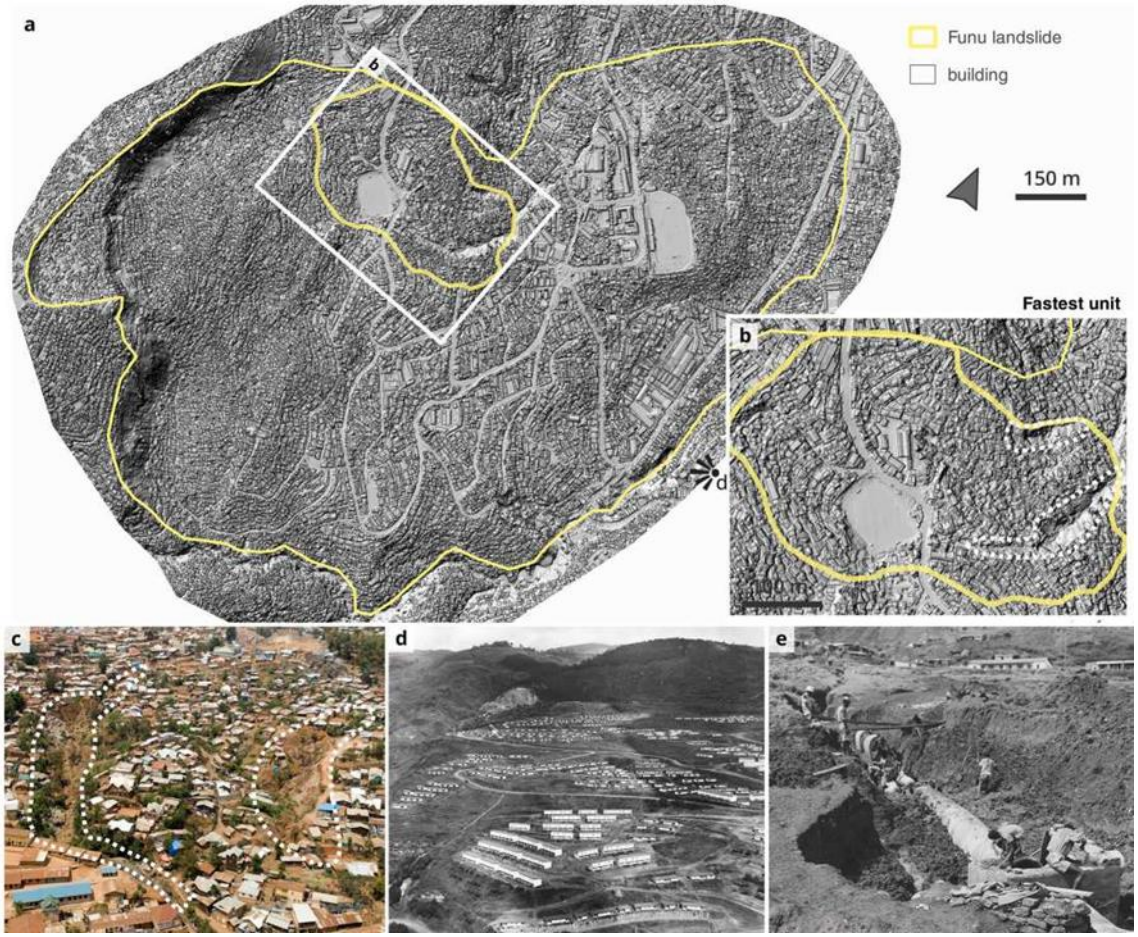

a, Very- high resolution shaded relief of the landslide from UAS-SfM (Oct. 2017). The resolution stresses the very-high density of individual building (the population is estimated to ~55 000 inhab./km^2 [4]). **b**, Funu landslide fastest unit, where characteristic landslide features (such as surface discontinuities, tension cracks, marked steps in slope profile) translating important internal deformation are the most visible. Two gullies (also shown in **c**,) delimit a sub-unit where velocities are the highest (up to 3 m/yr). **d**, Historical picture showing part of Funu landslide in 1959. It highlights the low housing density at that time. **e**, Illustrates work on the drainage systems in Bukavu (photo taken in 1959). © Royal Museum for Central Africa.

Published in : Nature Geoscience (2022), vol. 15, pp. 1048-1055
DOI: 10.1038/s41561-022-01073-3
Status : Postprint (Author's version)

References

1. Seto, K. C., Fragkias, M., Gu, B. & Reilly, M. K. A meta-analysis of global urban land expansion. *PLoS ONE* https://doi.org/10.1371/ journal.pone.0023777 (2011).
2. Ramalho, C. E. & Hobbs, R. J. Time for a change: dynamic urban ecology. *Trends Ecol. Evol.* **27**, 179-188 (2012).
3. Pelling, M. *The Vulnerability of Cities: Natural Disasters and Social Resilience* (Routledge, 2003).
4. Ozturk, U. et al. How climate change and unplanned urban sprawl bring more landslides.*Nature* **608**, 262-265 (2022).
5. Alexander, D. Urban landslides. *Prog. Phys. Geogr.* **13**, 157-189 (1989).
6. Schuster, R. L. & Highland, L. M. The third Hans Cloos lecture. Urban landslides: socioeconomic impacts and overview of mitigative strategies. *Bull. Eng. Geol. Environ.* **66**, 1-27 (2007).
7. Larsen, M. C. Rainfall-triggered landslides, anthropogenic hazards, and mitigation strategies. *Adv. Geosci.* **14**, 147-153 (2008).
8. Aleotti, P. & Chowdhury, R. Landslide hazard assessment summary review and new perspectives. *Bull. Eng. Geol. Environ.* **58**, 21-44 (1999).
9. Carey, J. M., Massey, C. I., Lyndsell, B. & Petley, D. N. Displacement mechanisms of slow-moving landslides in response to changes in porewater pressure and dynamic stress. *Earth Surf. Dyn.* **7**, 707-722 (2019).
10. Lacroix, P., Handwerger, A. L. & Bièvre, G. Life and death of slow-moving landslides. *Nat. Rev. Earth Environ.* **1**, 404-419 (2020).
11. Iverson, R. M. & Major, J. J. Rainfall, ground-water flow, and seasonal movement at Minor Creek landslide, northwestern California: physical interpretation of empirical relations. *Geol. Soc. Am. Bull.* **99**, 579-594 (1987).
12. Hilley, G., Bürgmann, R., Ferretti, A., Rocca, F. & Novali, F. Dynamics of slow-moving landslides from permanent scatterer analysis. *Science* **304**, 1952-1955 (2004).
13. Handwerger, A. L., Roering, J. J. & Schmidt, D. A. Controls on the seasonal deformation of slow-moving landslides. *Earth Planet. Sci. Lett.* **377-378**, 239-247 (2013).
14. Bennett, G. L. et al. Historic drought puts the brakes on earthflows in Northern California. *Geophys. Res. Lett.* **43**, 5725-5731 (2016).
15. Handwerger, A. L., Huang, M.-H. H., Fielding, E. J., Booth, A. M. & Bürgmann, R. A shift from drought to extreme rainfall drives a stable landslide to catastrophic failure. *Sci. Rep.* **9**, 1569 (2019).
16. Lacroix, P., Berthier, E. & Maquerhua, E. T. Earthquake-driven acceleration of slow-moving landslides in the Colca valley, Peru, detected from Pléiades images. *Remote Sens. Environ.* **165**, 148-158 (2015).
17. Bontemps, N., Lacroix, P., Larose, E., Jara, J. & Taipe, E. Rain and small earthquakes maintain a slow-moving landslide in a persistent critical state. *Nat. Commun.* **11**, 780 (2020).
18. Booth, A. M. et al. Transient reactivation of a deep-seated landslide by undrained loading captured with repeat airborne and terrestrial lidar. *Geophys. Res. Lett.* **45**, 4841-4850 (2018).

Published in : Nature Geoscience (2022), vol. 15, pp. 1048-1055
DOI: 10.1038/s41561-022-01073-3
Status : Postprint (Author's version)

19. Schulz, W. H., Kean, J. W. & Wang, G. Landslide movement in southwest Colorado triggered by atmospheric tides. *Nat. Geosci.* **2**, 863-866 (2009).

20. Iverson, R. M. Landslide triggering by rain infiltration. *Water Resour. Res.* **36**, 1897-1910 (2000).

21. Petley, D. N., Carey, J. M., Ng, K.-Y., Massey, C. I. & Froude, M. J. Understanding patterns of movement for slow moving landslides. In *Proc. 20th Symposium of the New Zealand Geotechnical Society* (eds Alexander, G. & Chin, C.) 1-11 (New Zealand Geotechnical Society, 2017).

22. Dille, A. et al. When image correlation is needed: unravelling the complex dynamics of a slow-moving landslide in the tropics with dense radar and optical time series. *Remote Sens. Environ.* **258**, 112402 (2021).

23. Lerner, D. N. Identifying and quantifying urban recharge: a review. *Hydrogeol. J.* **10**, 143-152 (2002).

24. Price, K. Effects of watershed topography, soils, land use, and climate on baseflow hydrology in humid regions: a review. *Prog. Phys. Geogr.* **35**, 465-492 (2011).

25. Fletcher, T. D., Andrieu, H. & Hamel, P. Understanding, management and modelling of urban hydrology and its consequences for receiving waters: a state of the art. *Adv. Water Resour.* **51**, 261-279 (2013).

26. Michellier, C. *Contribution to Geo-Risk Prevention: Population VulnerabilityAssessment in a Data Scarcity Context. Case Studies of Goma and Bukavu Cities (DR Congo)* (Université Libre de Bruxelles - Vrije Universiteit Brussel, 2017).

27. Overbeek, F. Van & Tamás, P. A. Autochthony and insecure land tenure: the spatiality of ethnicized hybridity in the periphery of post-conflict Bukavu, DRC. *J. East. Afr. Stud.* **12**, 290-309 (2018).

28. Hoffmann, K., Pouliot, M. & Muzalia, G. *Constructed Anarchy: Governance, Conflict, and Precarious Property Rights in Bukavu, Democratic Republic of the Congo* (SSRC, 2019)..

29. Moeyersons, J. et al. A geomorphological assessment of landslide origin at Bukavu, Democratic Republic of the Congo. *Eng. Geol.* **72**, 73-87 (2004).

30. Thomas, M. F. *Geomorphology in the Tropics: A Study of Weathering and Denudation in Low Latitudes* (John Wiley & Sons, 1994).

31. Dille, A. et al. Causes and triggers of deep-seated hillslope instability in the tropics—insights from a 60-year record of Ikoma landslide (DR Congo). *Geomorphology* **345**, 106835 (2019).

32. Dewitte, O. et al. Constraining landslide timing in a data-scarce context: from recent to very old processes in the tropical environment of the North Tanganyika-Kivu Rift region. *Landslides* **18**, 161-177 (2021).

33. Jaboyedoff, M. et al. in *Landslides and Engineered Slopes. Experience, Theory and Practice* (eds Avresa, S. et al.) 217-232 (CRC Press, 2016).

34. Samsonov, S. & d'Oreye, N. Multidimensional time-series analysis of ground deformation from multiple InSAR data sets applied to Virunga Volcanic Province. *Geophys. J. Int.* **191**, 1095-1108 (2012).

35. Samsonov, S., Dille, A., Dewitte, O., Kervyn, F. & D'Oreye, N. Satellite interferometry for mapping surface deformation time series in one, two and three dimensions: a new method illustrated on a slow-moving landslide. *Eng. Geol.* **266**, 105471 (2020).

36. Nobile, A. et al. Multi-temporal DInSAR to characterise landslide ground deformations in a tropical urban environment: focus on Bukavu (DR Congo). *Remote Sens.* **10**, 626 (2018).

37. Balegamire, C. et al. Vulnerability of buildings exposed to landslides: a spatio-temporal assessment in Bukavu (DR Congo). *Geo. Eco. Trop.* **41**, 263-278 (2017).

38. Krzeminska, D. M., Bogaard, T. A., Malet, J. P. & Van Beek, L. P. H. A model of hydrological and mechanical feedbacks of preferential fissure flow in a slow-moving landslide. *Hydrol. Earth Syst. Sci.* **17**, 947-959 (2013).

39. Schulz, W. H. et al. Landslide kinematics and their potential controls from hourly to decadal timescales: insights from integrating ground-based InSAR measurements with structural maps and long-term monitoring data. *Geomorphology* **285**, 121-136 (2017).

40. Van Asch, T. W. J., Buma, J. & Van Beek, L. P. H. A view on some hydrological triggering systems in landslides. *Geomorphology* **30**, 25-32 (1999).

41. Schulz, W. H., McKenna, J. P., Kibler, J. D. & Biavati, G. Relations between hydrology and velocity of a continuously moving landslide—evidence of pore-pressure feedback regulating landslide motion? *Landslides* **6**, 181-190 (2009).

42. Nereson, A. L., Davila Olivera, S. & Finnegan, N. J. Field and remote-sensing evidence for hydro-mechanical isolation of a long-lived earthflow in Central California. *Geophys. Res. Lett.* **45**, 9672-9680 (2018).

43. Malet, J.-P., Maquaire, O. & Calais, E. The use of global positioning system techniques for the continuous monitoring of landslides: application to the Super-Sauze earthflow (Alpes-de-Haute-Provence, France). *Geomorphology* **43**, 33-54 (2002).

44. Massey, C. I., Petley, D. N. & McSaveney, M. J. Patterns of movement in reactivated landslides. *Eng. Geol.* **159**, 1-19 (2013).

45. Corominas, J., Moya, J., Ledesma, A., Lloret, A. & Gili, J. A. Prediction of ground displacements and velocities from groundwater level changes at the Vallcebre landslide (Eastern Pyrenees, Spain). *Landslides* **2**, 83-96 (2005).

46. Sidle, R. C. & Bogaard, T. A. Dynamic Earth system and ecological controls of rainfall-initiated landslides. *Earth. Sci. Rev.* **159**, 275-291 (2016).

47. Sidle, R. C. & Ochiai, H. *Landslides: Processes, Prediction, and Land Use* (American Geophysical Union, 2006).

48. Ollier, C., Calcaterra, D. & Parise, M. Studies in weathering and slope movements—an introduction. *Geomorphology* **87**, 101-103 (2007).

49. Fan, X. et al. Earthquake-induced chains of geologic hazards: patterns, mechanisms, and impacts. *Rev. Geophys.* **57**, 421-503 (2019).

50. Bogaard, T. A. & Greco, R. Landslide hydrology: from hydrology to pore pressure. *Wiley Interdiscip. Rev. Water* **3**, 439-459 (2016).

51. Holcombe, E. A., Beesley, M. E. W., Vardanega, P. J. & Sorbie, R. Urbanisation and landslides: hazard drivers and better practices. *Proc. Inst. Civ. Eng.* **169**, 137-144 (2016).

Published in : Nature Geoscience (2022), vol. 15, pp. 1048-1055
DOI: 10.1038/s41561-022-01073-3
Status : Postprint (Author's version)

52. Omondi, P. A. et al. Changes in temperature and precipitation extremes over the Greater Horn of Africa region from 1961 to 2010. *Int. J. Climatol.* **34**, 1262-1277 (2014).

53. Souverijns, N., Thiery, W., Demuzere, M. & Lipzig, N. P. M. V. Drivers of future changes in East African precipitation. *Environ. Res. Lett.* **11**, 114011 (2016).

54. IPCC *Climate Change 2021: The Physical Science Basis* (eds Masson-Delmotte, V. et al.) (Cambridge Univ. Press, 2021).

55. Agliardi, F., Scuderi, M. M., Fusi, N. & Collettini, C. Slow-to-fast transition of giant creeping rockslides modulated by undrained loading in basal shear zones. *Nat. Commun.* **11**, 1352 (2020).

56. Satterthwaite, D., Huq, S., Pelling, M., Hannah R. & Lankao, P. R. *Adapting to Climate Change in Urban Areas: The Possibilities and Constraints in Low- and Middle-Income Nations* (IIED, 2007).

57. Anderson, M. G. & Holcombe, E. *Community-Based Landslide Risk Reduction* (World Bank, 2013).

58. Depicker, A. et al. The added value of a regional landslide susceptibility assessment: the western branch of the East African Rift. *Geomorphology* **353**, 17 (2020).

59. Derauw, D. Phasimétrie par Radar à Synthèse d'Ouverture; Théorie et Applications (Université de Liège, 1999).

60. d'Oreye, N., Derauw, D., Samsonov, S., Jaspard, M. & Smittarello, D. MasTer: a full automatic multi-satellite InSAR mass processing tool for rapid incremental 2D ground deformation time series. In *Proc. International Geoscience and Remote Sensing Symposium*, 1899-1902 (IEEE, 2021).

61. Derauw, D., d'Oreye, N., Jaspard, M., Caselli, A. & Samsonov, S. Ongoing automated ground deformation monitoring of Domuyo—Laguna del Maule area (Argentina) using Sentinel-1 MSBAS time series: methodology description and first observations for the period 2015-2020. *J. South Am. Earth Sci.* **104**, 102850 (2020).

62. Tadono, T. et al. Generation of the 30 m-mesh global digital surface model by ALOS PRISM. *Int. Arch. Photogramm. Remote Sens. Spat. Inf. Sci.* **XLI-B4**, 157-162 (2016).

63. Rupnik, E., Daakir, M. & Pierrot-Deseilligny, M. MicMac - a free, open-source solution for photogrammetry. *Open Geospat. Data Softw. Stand.* **2**, 14 (2017).

64. Eltner, A. et al. Image-based surface reconstruction in geomorphometry—merits, limits and developments. *Earth Surf. Dyn.* **4**, 359-389 (2016).

65. James, M. R. & Robson, S. Mitigating systematic error in topographic models derived from UAV and ground-based image networks. *Earth Surf. Process. Landf.* **39**, 1413-1420 (2014).

66. *Agisoft Metashape Pro* (Agisoft, 2020).

67. Cook, K. L. & Dietze, M. Short communication: a simple workflow for robust low-cost UAV-derived change detection without ground control points. *Earth Surf. Dyn.* **7**, 1009-1017 (2019).

68. Leprince, S., Ayoub, F., Klinger, Y. & Avouac, J. P. Co-registration of optically sensed images and correlation (COSI-Corr): an operational methodology for ground deformation measurements. In *Proc. International Geoscience and Remote Sensing Symposium*, 1943-1946 (IEEE, 2007).

69. Fleming, R. W., Baum, R. L. & Giardino, M. *Map and Description of the Active Part of the Slumgullion Landslide, Hinsdale County, Colorado, US Department of the Interior, US Geological Survey* (1999).

Published in : Nature Geoscience (2022), vol. 15, pp. 1048-1055
DOI: 10.1038/s41561-022-01073-3
Status : Postprint (Author's version)

70. Parise, M. Observation of surface features on an active landslide, and implications for understanding its history of movement. *Nat. Hazards Earth Syst. Sci.* **3**, 569-580 (2003).

71. Dewitte, O. & Demoulin, A. Morphometry and kinematics of landslides inferred from precise DTMs in West Belgium. *Nat. Hazards Earth Syst. Sci.* **5**, 259-265 (2005).

72. Samsonov, S. & D'Oreye, N. Multidimensional small baseline subset (MSBAS) for two-dimensional deformation analysis: case study Mexico City. *Can. J. Remote Sens.* **43**, 318-329 (2017).

73. Keefer, D. K. Investigating landslides caused by earthquakes—a historical review. *Surv. Geophys.* **23**, 473-510 (2002).

74. Delvaux, D. et al. Seismic hazard assessment of the Kivu rift segment based on a new seismotectonic zonation model (western branch, East African Rift system). *J. Afr. Earth Sci.* **134**, 831-855 (2017).

75. Oth, A. et al. KivuSNet: the first dense broadband seismic network for the Kivu rift region (western branch of East African Rift). *Seismol. Res. Lett.* **88**, 49-60 (2017).

76. *Earthquake Hazards Program* (USGS, 2020); https://earthquake. usgs.gov/

77. Huffman, G., Bolvin, D., Braithwaite, D., Hsu, K. & Joyce, R. *NASA Global Precipitation Measurement—Integrated Multi-satellite Retrievals for GPM* Algorithm Theoretical Basis Document v.06 (NASA, 2019).

78. Monsieurs, E. *The Potential of Satellite Rainfall Estimates in Solving Regional Landslide Hazard Modelling in Data-Scarce Contexts* (Royal Museum for Central Africa/Université de Liège, 2020).

79. Baum, R. L., Messerich, J. & Fleming, R. W. Surface deformation as a guide to kinematics and three-dimensional shape of slow-moving, clay-rich landslides, Honolulu, Hawaii. *Environ. Eng. Geosci.* **4**, 283-306 (1998).

80. Bakker, M. & Lane, S. N. Archival photogrammetric analysis of river-floodplain systems using structure from motion (SfM) methods. *Earth Surf. Process. Landf.* **42**, 1274-1286 (2017).

81. Dewitte, O. et al. Tracking landslide displacements by multi-temporal DTMs: a combined aerial stereophotogrammetric and LIDAR approach in western Belgium. *Eng. Geol.* **99**, 11-22 (2008).

82. Fairfield, J. & Leymarie, P. Drainage networks from grid digital elevation models. *Water Resour. Res.* **27**, 709-717 (1991).

83. Trefois, P. et al. *Géologie urbaine de Bukavu: interaction entre la stabilité du sol et la pression démographique.* (UNESCO, 2003).

84. Kalikone Buzera, C. et al. Ground deformation impact on the vulnerability of water and electricity distribution networks in Bukavu (DR Congo). *Geo. Eco. Trop.* **41**, 279-292 (2017).